

CINTAL - Centro de Investigação Tecnológica do Algarve

Universidade do Algarve

**Study and implementation of
bubbles size distribution estimation
method applied to marine plant monitoring**

Jef PHILIPPINE

Rep 04/18 - SiPLAB
31/05/2018

University of Algarve
Campus de Gambelas
8005-139, Faro
Portugal

tel: +351-289800131
fax: +351-289864258
cintal@ualg.pt
www.ualg.pt/cintal

Work requested by	CINTAL Universidade do Algarve, FCT - Campus de Gambelas 8005-139 Faro, Portugal Tel/Fax: +351-289864258, cintal@ualg.pt, www.cintal.ualg.pt
Laboratory performing the work	SiPLAB - Signal Processing Laboratory Universidade do Algarve, Campus de Gambelas, 8005-139 Faro, Portugal tel: +351-289800949, info@siplab.fct.ualg.pt, www.siplab.fct.ualg.pt
Project	SEAOX (PTDC/EEIPRO/2598/2014)
Title	Study and implementation of bubbles size distribution estimation method applied to marine plant monitoring
Authors	Jef PHILIPPINE (jef.philippine@grenoble-inp.org)
Date	Mai 31, 2018
Reference	04/18 - SiPLAB
Number of pages	81
Abstract	This report presents the work carried out from 1st December 2017 to 31st Mai 2018 under SEAOX project. It aimed to study the feasibility of scattering-based methods for bubbles monitoring, applied to marine plants production. Backscattering theory is first considered, based on the operation of a sediment monitoring device, adapted to project goals for the occasion. The second studied option aims to make underwater sound speed and attenuation measurements for a set of frequencies in order to access the characteristics of the bubbly medium. Both theories and experimental results are presented and documented in this report, that will support further investigations.
Clearance level	UNCLASSIFIED
Distribution list	SiPLAB, CINTAL
Total number of recipients	

Abstract

This report presents the work carried out from 1st December 2017 to 31st Mai 2018 under SEAOX project. It aimed to study the feasibility of scattering-based methods for bubbles monitoring, applied to marine plants production. Backscattering theory is first considered, based on the operation of a sediment monitoring device, adapted to project goals for the occasion. The second studied option aims to make underwater sound speed and attenuation measurements for a set of frequencies in order to access the characteristics of the bubbly medium. Both theories and experimental results are presented and documented in this report, that will support further investigations.

Acknowledgments

The author thanks technical staff at IPMA-EPPO for providing the experiments site. This work was funded by National Funds through FCT-Foundation for Science and Technology under project SEAUX (PTDC/EEIPRO/2598/2014).



Contents

Abstract	III
Acknowledgments	IV
List of Figures	VIII
Introduction	7
I Backscattering and high frequency methods	8
1 Sonar equation	10
1.1 In terms of pressure	10
1.2 In terms of voltages	17
1.3 About the attenuation term	17
2 Directivity, beamwidth and insonified volume	20
2.1 Directivity and beamwidth	20
2.2 Integrated beam pattern	21
2.3 Insonified volume and resolution	22
3 Extracting data from the device	23
3.1 Device short presentation	23
3.2 IPMA set of data	24
3.3 Rewriting the equations	25
3.4 Auto-calibration method	27

3.5	Accessing the backscattering cross-section per volum unit	29
3.6	About near field correction	29
4	Calibration experiment	31
4.1	Overview of experimental setup	31
4.2	Experimental data	33
4.3	Processing the data	39
4.4	Further calibration work	40
5	Backscattering cross-section distribution	41
5.1	Extinction cross-section	41
5.2	How to isolate M_v and $10^{-2 \cdot att}$	42
5.3	Bubble size distribution	42
5.4	Cross-section and damping constants: first formulas	43
5.5	Cross-section and damping constants: second and final formulas	46
5.6	Distribution and cross-section per unit volume	48
	Conclusion on high frequency methods	51
II	Attenuation, sound-speed and low frequency methods	52
6	Theoretical background	54
6.1	Dispersion equation and complex sound speed	54
6.2	u and v calculation	55
7	Kernel inversion process	57
7.1	Discretisation	57
7.2	Matrix-form writing	58
7.3	Problem inversion	59
8	Case study: [20-90] kHz measurement band	61
8.1	Shape of Q_1 and Q_2	61

8.2	Frequency and radius	62
8.3	Inversion processes	63
	Conclusion on low frequency methods	69
III	Appendix, notations, Matlab files and bibliography	70
	Notations	74
	Matlab files	77
	Bibliography	80

List of Figures

1.1	Geometry of the backscattering	10
1.3	Attenuation coefficient α_w over water temperature Θ	18
1.4	Attenuation term from water over range	18
2.1	Theoretical directivity patterns	21
2.2	Insonified volume illustration	22
3.1	IPMA 2016 data - Signal received from surface	24
3.2	IPMA 2016 data - Signal received - Time evolution	26
3.3	IPMA 2016 data - Raw signal	26
3.4	IPMA 2016 data - “Decompensated” signal	26
3.5	Calibration setup	28
3.6	Near range factor ξ	30
4.1	Tank and working table	31
4.2	Device in the empty tank	31
4.3	Device in the tank (close view)	32
4.4	Noise for $L = 2.5$ mm	35
4.5	Signal for $L = 2.5$ mm	35
4.6	Noise for $L = 10$ mm	36
4.7	Signal for $L = 10$ mm	36
4.8	Noise for $L = 40$ mm	37
4.9	Signal for $L = 40$ mm	37
4.10	Signal for $L = 2.5$ mm (focus on surface range)	38

4.11	Signal for $L = 40$ mm (focus on surface range)	38
4.12	Signal (dB) for $L = 2.5$ mm (focus on surface range)	39
4.13	Signal (dB) for $L = 10$ mm (focus on surface range)	39
5.1	Damping constant absolute value	45
5.2	Scattering cross-section according to particle radius	45
5.3	Scattering cross-section comparison	46
5.4	Scattering cross-section for all ka , incomplete	46
5.5	Scattering cross-section for all ka	47
5.6	Extinction cross-section for all ka	47
5.7	Cross-sections ratio	48
6.1	Low-frequency experimental setup	56
8.1	Specific shapes of Q_1 and Q_2	61
8.2	Specific shapes of Q_1 and Q_2 for different values of q_v	62
8.3	Kernel K_1 for a large radius range	63
8.4	Kernel K_2 for a large radius range	63
8.5	Kernel K_1 for a radius range centered on the resonating radius	64
8.6	Kernel K_2 for a radius range centered on the resonating radius	64
8.7	Q_1 and Q_2 shapes for a normal distribution centered on $30 \mu\text{m}$	64
8.8	Q_1 and Q_2 shapes for a normal distribution centered on $140 \mu\text{m}$	65
8.9	Set of distributions for inversion	65
8.10	Correlation coefficients ρ over M for distribution of case 1	66
8.11	Correlation coefficients ρ over M for distribution of case 2	66
8.12	Correlation coefficients ρ over M for distribution of case 3	66
8.13	Correlation coefficients ρ over M for distribution of case 1, with noise	67
8.14	Correlation coefficients ρ over M for distribution of case 2, with noise	67
8.15	Correlation coefficients ρ over M for distribution of case 3, with noise	68
8.16	Near range factor ξ	73

Introduction

Under the supervision of prof. Paulo FELISBERTO from SiPLAB (University of Algarve), the SEAUX project aims to measure oxygen bubbles production by seagrass in shallow water. Bubble population parameters such as void fraction (i.e the ratio oxygen/water in a given volume) or distribution according to bubble size are of interest. The first idea to achieve the project goals was using an acoustic backscatter system (ABS, originally conceived to measure sediment concentration) in order to get informations on the bubbly medium. For this purpose, the ABS needed to be characterized and calibrated, since the available information were not very precise and needed to be extended, then methods had to be developed to determine O₂ bubbles concentration. The first part of the present report deals with this method, so-called "Backscattering and high-frequency methods", due to the frequencies in operation (MHz order). The second idea came from an on-going project led by Paulo FELISBERTO and João PARENTE. It aims to measure attenuation and sound speed variation through a bubbly medium for lower frequencies (kHz order), then access the distribution via these measurements. The complete set-up and theory are not described in this report, and one must read [1] to fully understand the necessary background. The second part of this report focuses on this method. As a result of the report structure, written alongside the work, most of the notations and objectives are detailed in the first part. In particular, it means that a quick reading of this first part is necessary to understand what the second part is about.

Notations are explained at the end of the document. When necessary, Matlab objects are indicated as `exemple_script.m`. A large amount of scripts has been written during these 6-months, full of comments and most of the time consistent in notations and functions. They can be used to plot again the different figures of this report.

Part I

Backscattering and high frequency methods

This part deals with the use of a backscattering device to measure the bubble size distribution in a given water volume. It starts with sonar equation theory, specifically derived for our application, then deals with directivity and beamwidth of the device, before going through extraction of data and calibration process. It ends with cross-sections and bubble distribution theory, that are needed in the second part.

An e-mail exchange with Andy SMERDON from AQUAtec support service is available under [Mail conversation - AQUAtec.pdf](#).

Even though this part has been the most important in terms of time during the 6-months contract, it seems difficult to draw accurate conclusions from the ABS device only. The main bottlenecks are the number of frequency not enough to extract information from the data and the high-frequencies engaged in the process, hardly adapted to measure the bubble size involved.

Chapter 1

Sonar equation

The following equations are adapted from [2] and deal with propagation, attenuation and backscattering. The time dependency is dropped in these equations, and for better visibility so is the frequency dependency. Spherical coordinates (r, θ, ϕ) are used, where r is the radius, θ the inclination and ϕ the azimuth.

Assume the source produces a sound pressure P_0 , defined at range $r = R_0 = 1 \text{ m}$. The directivity pattern of the source is $D_t(\theta, \phi)$ (chapter 2 deals with this directivity). Figure 1.1 shows the geometry of the situation.

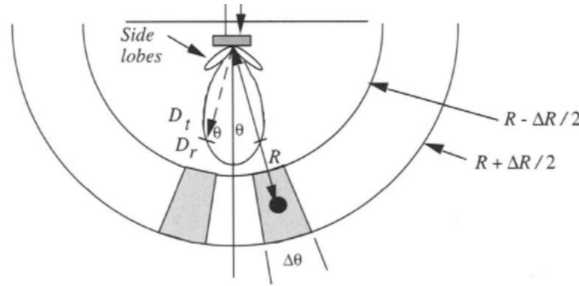


Figure 1.1: Geometry of the situation. Image from [2, p. 439].
 ΔR is equivalent to L in this report

1.1 In terms of pressure

The incident pressure $P_s(r, \theta, \phi)$ for a spherical wave is adapted from [2, p. 139]. The theory of backscattering must be known in order to understand the following.

$$P_s(r, \theta, \phi) = P_0 D_t(\theta, \phi) \frac{R_0}{r} 10^{-\frac{\alpha_w(r-R_0)}{20}} 10^{-0.217B_t(r, \theta, \phi)} \quad (1.1)$$

where α_w is the attenuation rate due to water as a lossy medium (see [2, p. 103]). B_t represents the attenuation due to bubbles. This last term is discussed further in the chapter. For better readability, let be $att(r, \theta, \phi) = \frac{\alpha_w(r-R_0) + 4.34B_t(r, \theta, \phi)}{20}$ the total attenuation.

Let be $|L_s(r, \theta, \phi)|$ the backscattering length at (r, θ, ϕ) and $P_{scat}(r, \theta, \phi)$ the scattered pressure. It comes from [2]

$$P_{scat}(r, \theta, \phi) = \frac{|L_s(r, \theta, \phi)|}{R_0} P_s(r, \theta, \phi) \quad (1.2)$$

The backscattered pressure is, as well, subject to attenuation and spherical divergence. Let be $dP_r(r, \theta, \phi)$ the pressure received by the transducer from an object situated in (r, θ, ϕ) , and $D_r(\theta, \phi)$ the directivity pattern of the receiver.

$$dP_r(r, \theta, \phi) = P_{scat}(r, \theta, \phi) D_r(\theta, \phi) \frac{R_0}{r} 10^{-att(r, \theta, \phi)} \quad (1.3)$$

Arranging equations 1.1, 1.2 and 1.3 leads to:

$$dP_r(r, \theta, \phi) = P_0 D_t(\theta, \phi) D_r(\theta, \phi) \frac{R_0}{r^2} |L_s(r, \theta, \phi)| 10^{-2 \cdot att(r, \theta, \phi)} \quad (1.4)$$

Equation 1.4 will now be squared to make the differential cross-section $\Delta\sigma_{BS}(r, \theta, \phi) = |L_s(r, \theta, \phi)|^2$ appear.

$$dP_r^2(r, \theta, \phi) = P_0^2 D_t^2(\theta, \phi) D_r^2(\theta, \phi) \frac{R_0^2}{r^4} \Delta\sigma_{BS}(r, \theta, \phi) 10^{-2 \cdot att(r, \theta, \phi)} \quad (1.5)$$

Assuming the scattering is omni-directional, the total backscattering cross-section $\sigma_{BS}(r, \theta, \phi)$, which is the integral of $\Delta\sigma_{BS}(r, \theta, \phi)$ over 4π of solid angle, can be written as (see [2, p. 238])

$$\sigma_{BS}(r, \theta, \phi) = 4\pi \Delta\sigma_{BS}(r, \theta, \phi) \quad (1.6)$$

Now, let be $d^3V(r, \theta, \phi)$ the spherical elementary volume. We can introduce the backscattering cross-section per unit volume $M_v(r, \theta, \phi)$ as

$$M_v(r, \theta, \phi) d^3V(r, \theta, \phi) = \sigma_{BS}(r, \theta, \phi) \quad (1.7)$$

Due to the device resolution L (see section 2.3), the total squared pressure $P_r^2(R)$ received by the transducer from range R is actually the continuous sum of signal from range $R - \frac{L}{2}$ to $R + \frac{L}{2}$ over the whole angles, defined as

$$P_r^2(R) = \int_{r=R-\frac{L}{2}}^{R+\frac{L}{2}} \int_{\theta=0}^{\frac{\pi}{2}} \int_{\phi=0}^{2\pi} dP_r^2(r, \theta, \phi) \quad (1.8)$$

Arranging equations 1.5 to 1.8 leads to equation 1.9. For visibility reasons, the writing is lightened.

$$P_r^2(R) = \frac{P_0^2 R_0^2}{4\pi} \iint_{\theta, \phi} D_t^2(\theta, \phi) D_r^2(\theta, \phi) \int_r M_v(r, \theta, \phi) \frac{1}{r^4} 10^{-2 \cdot att(r, \theta, \phi)} d^3V \quad (1.9)$$

1.1.1 Dealing with the range integration

In order to integrate equation 1.9, some assumptions have to be done:

1. $L \ll R$
2. M_v is supposed to be constant over range $R - \frac{L}{2}$ to $R + \frac{L}{2}$, so that $M_v(r, \theta, \phi) = M_v(R, \theta, \phi)$,
3. The water attenuation term $10^{-2 \cdot att(r, \theta, \phi)}$ is supposed to be constant over range $R - \frac{L}{2}$ to $R + \frac{L}{2}$,

The second and third assumptions allow to take the terms out of the range integration. The first one allows to replace r^{-4} with R^{-4} (see Appendix). Equation 1.9 can then be rewritten as

$$P_r^2(R) = P_0^2 \frac{R_0^2}{R^4} \frac{1}{4\pi} \iint_{\theta, \phi} D_t^2(\theta, \phi) D_r^2(\theta, \phi) 10^{-2 \cdot att(R, \theta, \phi)} M_v(R, \theta, \phi) \int_{r=R-\frac{L}{2}}^{R+\frac{L}{2}} d^3V \quad (1.10)$$

The range integration is then

$$\begin{aligned} \int_{r=R-\frac{L}{2}}^{R+\frac{L}{2}} d^3V &= \sin \theta d\theta d\phi \int_{r=R-\frac{L}{2}}^{R+\frac{L}{2}} r^2 dr \\ &= \frac{1}{3} \left(\left(R + \frac{L}{2}\right)^3 - \left(R - \frac{L}{2}\right)^3 \right) \sin \theta d\theta d\phi \\ &= V_G(R) \sin \theta d\theta d\phi \end{aligned} \quad (1.11)$$

One can notice that $\sin \theta d\theta d\phi$ is the elementary solid angle. It leads to

$$P_r^2(R) = P_0^2 \frac{R_0^2}{R^4} \frac{V_G(R)}{4\pi} \iint_{\theta, \phi} M_v(R, \theta, \phi) D_t^2(\theta, \phi) D_r^2(\theta, \phi) 10^{-2 \cdot att(R, \theta, \phi)} \sin \theta d\theta d\phi \quad (1.12)$$

The integral part of the previous equation can be rewritten as (everything is supposed to be independent from ϕ):

$$\begin{aligned} &\iint_{\theta, \phi} M_v(R, \theta, \phi) D_t^2(\theta, \phi) D_r^2(\theta, \phi) 10^{-2 \cdot att(R, \theta, \phi)} d^3V \\ &= 2\pi \int_{\theta} M_v(R, \theta) D_t^2(\theta) D_r^2(\theta) 10^{-2 \cdot att(R, \theta)} \sin \theta d\theta \end{aligned} \quad (1.13)$$

Without any other assumption, the integral cannot be easily solved. In the following are discussed different possible simplifications. It is anyway supposed that, in our case, the two directivities are the same, so that $D_t^2 D_r^2 = D_t^4$.

1.1.2 Window assumption on D_t^4

A simplification is proposed in [3]: “the actual two-way beam pattern $[D_t^4]$ can be replaced by an ideal pattern of unit-relative response within solid angle $[\theta_{mx}]$, and zero relative response beyond $[\theta_{mx}]$.” Product D_t^4 is thus supposed to hold the following assumption:

$$D_t^4(\theta) = \begin{cases} 1 & \text{if } 0 < \theta < \theta_{mx} \\ 0 & \text{if } \theta_{mx} < \theta < \frac{\pi}{2} \end{cases} \quad (1.14)$$

The angle θ_{mx} actually defines an effective solid angle and can be chosen according to different possibilities. Validity of this strong assumption is not discussed at all in [3], but has been seen somewhere else in literature (reference is lost). It allows equation 1.13 to be simplified as

$$\begin{aligned} & 2\pi \int_{\theta} M_v(R, \theta) D_t^4(\theta) 10^{-2 \cdot att(R, \theta)} \sin \theta d\theta \\ &= 2\pi \int_{\theta=0}^{\theta_{mx}} M_v(R, \theta) 10^{-2 \cdot att(R, \theta)} \sin \theta d\theta \end{aligned} \quad (1.15)$$

Figure 1.2 shows the real function D_t^4 and the windows from two approximations (hypothesis 1 and 2). To be free from the frequency parameter, the x-axis is $kA_t \sin \theta$ (see section 2.1), where k is the wave number and A_t the considered transducer radius.

Hypothesis 1

The integration of $D_t^4(\theta)$ over $[0, \frac{\pi}{2}]$ is kept :

$$\int_{\theta=0}^{\frac{\pi}{2}} D_{t,real}^4(\theta) d\theta = \int_{\theta=0}^{\theta_{mx}} D_{t,hyp.1}^4(\theta) d\theta \quad (1.16)$$

It leads to

$$\theta_{mx,hyp.1} = \int_{\theta=0}^{\frac{\pi}{2}} D_t^4(\theta) d\theta \quad (1.17)$$

Hypothesis 2

The integration of $D_t^4(\theta) \sin \theta$ over $[0, \frac{\pi}{2}]$ is kept. This hypothesis allows to make the integrated beam pattern ψ from [2] appear (see section 2.2):

$$\int_{\theta=0}^{\frac{\pi}{2}} D_{t,real}^4(\theta) \sin \theta d\theta = \int_{\theta=0}^{\theta_{mx}} D_{t,hyp.2}^4(\theta) \sin \theta d\theta \quad (1.18)$$

It leads to

$$\theta_{mx,hyp.2} = \arccos\left(1 - \frac{\psi}{2\pi}\right) \quad (1.19)$$

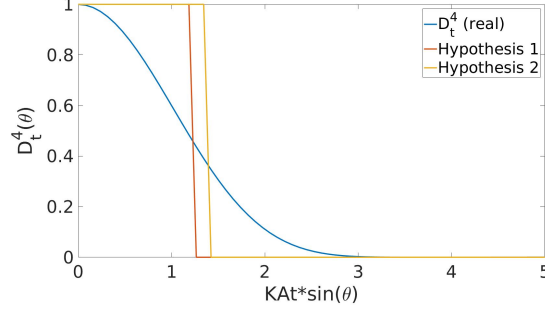


Figure 1.2: $D_t^4(\theta)$ (real and approximated)

As shown in figure 1.2, these approximation are strong and globally wrong. They allow to define a solid angle on which M_v can be considered as constant. The integration is then simplified and possible. Other hypothesis could be formulated: for instance, θ_{mx} can be defined as the -3 dB beamwidth for each frequency (see section 2.1).

1.1.3 After window assumptions on D_t^4

Once assumptions on D_t^4 are done, a second assumption is to be made:

$$M_v(R, \theta) 10^{-2 \cdot att(R, \theta)} = M_v(R) 10^{-2 \cdot att(R)} \quad \text{for } \theta \in [0, \theta_{mx}] \quad (1.20)$$

This assumption only means that the backscattering cross-section per unit volume is constant over the insonified volume defined by $[0, \theta_{mx}]$, and so is the attenuation term. Equation 1.13 can then be simplified as

$$\begin{aligned} & 2\pi \int_{\theta=0}^{\frac{\pi}{2}} M_v(R, \theta) D_t^4(\theta) 10^{-2 \cdot att(R, \theta)} \sin \theta d\theta \\ &= 2\pi M_v(R) 10^{-2 \cdot att(R)} \int_{\theta=0}^{\theta_{mx}} \sin \theta d\theta \\ &= 2\pi M_v(R) 10^{-2 \cdot att(R)} (1 - \cos \theta_{mx}) \end{aligned} \quad (1.21)$$

where $2\pi (1 - \cos \theta_{mx})$ is called ideal beam pattern ψ_{BP} and is a solid angle.

1.1.4 Another proposed assumption

Another approximation to calculate the integral part of equation 1.13 is formulated below:

Hypothesis 3

Figure 1.2 shows that $D_t^4(\theta)$ is zero for $kA_t \sin \theta = 3$ (to be precise, D_t^4 is 0.0026 at this point). The angle θ_{mx} is calculated as

$$kA_t \sin \theta_{mx} = 3 \quad (1.22)$$

which leads to

$$\theta_{mx,hyp.3} = \arcsin\left(\frac{3}{kA_t}\right) \quad (1.23)$$

NOTE In our case $kA_t > 10$, so $\frac{3}{kA_t} < 1$ so \arcsin function is correctly defined.

It is then assumed that $M_v(R, \theta) 10^{-2 \cdot att(R, \theta)}$ is constant over the insonified volume defined by $[0, \theta_{mx,hyp.3}]$ (same as equation 1.20). It leads to

$$\begin{aligned} & 2\pi \int_{\theta=0}^{\frac{\pi}{2}} M_v(R, \theta) D_t^4(\theta) 10^{-2 \cdot att(R, \theta)} \sin \theta d\theta \\ &= M_v(R) 10^{-2 \cdot att(R)} 2\pi \int_{\theta=0}^{\theta_{mx,hyp.3}} D_t^4(\theta) \sin \theta d\theta \\ &\approx M_v(R) 10^{-2 \cdot att(R)} 2\pi \int_{\theta=0}^{\frac{\pi}{2}} D_t^4(\theta) \sin \theta d\theta \\ &\approx M_v(R) 10^{-2 \cdot att(R)} \psi \end{aligned} \quad (1.24)$$

With this formalism, the integrated beam-pattern ψ from [2] is used and a reasonable solid angle is defined for the device. The insonified volume where M_v is constant is then defined as

$$\begin{aligned} V_{ins}(R) &= 2\pi V_G(R) \int_{\theta=0}^{\theta_{mx,hyp.3}} \sin \theta d\theta \\ &= 2\pi V_G(R) (1 - \cos \theta_{mx,hyp.3}) \\ &= 2\pi V_G(R) \left(1 - \cos \arcsin\left(\frac{3}{kA_t}\right)\right) \\ &= 2\pi V_G(R) \left(1 - \sqrt{1 - \frac{9}{(kA_t)^2}}\right) \\ &\approx 2\pi LR^2 \left(1 - \sqrt{1 - \frac{9}{(kA_t)^2}}\right) \end{aligned} \quad (1.25)$$

1.1.5 Conclusion on the pressure equation

Whichever assumption is made from previously presented hypothesis, equation 1.9 can now be rewritten as

$$P_r^2(R) = P_0^2 \frac{R_0^2}{R^4} \frac{M_v(R)}{4\pi} \psi_{BP} V_G(R) 10^{-2 \cdot att(R)} \quad (1.26)$$

NOTE Even though the previous methods allows to make the volume V_G appears, it leads to a possible misunderstanding when reading the equation, because $V_G(R) \propto R^2$. For this reason, if r^{-4} is not replaced with R^{-4} in the range integration (equation 1.11), it leads to (see

Appendix)

$$\begin{aligned} \int_{r=R-\frac{L}{2}}^{R+\frac{L}{2}} \frac{1}{r^4} d^3V &= \sin\theta d\theta d\phi \int_{r=R-\frac{L}{2}}^{R+\frac{L}{2}} \frac{1}{r^2} dr \\ &= \frac{L}{R^2} \sin\theta d\theta d\phi \end{aligned} \quad (1.27)$$

The same result can be found with $V_G(R) \approx LR^2$ (equivalent for $R \gg \frac{L}{2}$). It leads to equation 1.28, the one that is used from now.

$$P_r^2(R) = P_0^2 \frac{R_0^2}{R^2} \frac{M_v(R)}{4\pi} \psi_{BP} L 10^{-2 \cdot att(R)} \quad (1.28)$$

Table 1.1 shows the values of ψ_{BP} and θ_{mx} according to which hypothesis is used. Of course, ψ_{BP} are the same for hypothesis 2 and 3, but the angle θ_{mx} are different. For more information, refer to chapter 2.

		Frequency (MHz)			
		0.5	1	2	4
ψ_{BP} [sr]	1	0.0073	0.0033	0.0029	0.0007
	Hypothesis 2	0.0092	0.0041	0.0036	0.0009
	3	0.0092	0.0041	0.0036	0.0009
	Hypothesis 2	0.0092	0.0041	0.0036	0.0009
θ_{mx} [rad]	1	0.0483	0.0322	0.0302	0.0149
	Hypothesis 2	0.0540	0.0360	0.0337	0.0166
	3	0.1197	0.0797	0.0747	0.0369
	Hypothesis 2	0.1197	0.0797	0.0747	0.0369

Table 1.1: ψ_{BP} and θ_{mx} according to hypothesis

Hypothesis 3 is applied from now and at every frequency, so that the ionized volume is as defined in equation 1.25, and

$$\psi_{BP}(f) = \psi(f)$$

and

$$\theta_{mx}(f) = \frac{3}{kA_t(f)}$$

1.2 In terms of voltages

Let us write v_s and $v_r(R)$, respectively the input voltage of the source and the output voltage of the receiver from an object situated at range R , and the gains G_s and K_r defined as

$$\begin{aligned} P_s &= G_s v_s \\ K_r P_r(R) &= v_r(R) \end{aligned} \tag{1.29}$$

The gain K_r takes into account all the gains applied by the device on the raw recorded signal. We can then write

$$\frac{v_r^2(R)}{K_r^2} = G_s^2 v_s^2 \frac{R_0^2}{R^2} \frac{M_v(R)}{4\pi} \psi L 10^{-2 \cdot att(R)} \tag{1.30}$$

Equation 1.30 can be written in logarithmic version as

$$RL = SL + TS - 2TL \tag{1.31}$$

with the following notations:

$$\begin{aligned} RL &= 10 \log_{10} v_r^2 - 10 \log_{10} K_r^2 \\ SL &= 10 \log_{10} v_s^2 + 10 \log_{10} G_s^2 \\ TS &= 10 \log_{10} \left(\frac{M_v(R)}{4\pi} \psi L \right) \\ TL &= 10 \log_{10} R - 10 \log_{10} R_0 + 10 \cdot att(R) \end{aligned} \tag{1.32}$$

This equation is the same as the one proposed in [3], with some differences in terms, in particular because the volume V_G has been removed. The next chapter deals with directivity and beamwidth.

1.3 About the attenuation term

As stated at the beginning of this chapter, the attenuation term depends both on water and bubbles.

1.3.1 Water attenuation

Aquatec provides in [4] the equation 1.33 to calculate the attenuation coefficient α_w . This equation only takes water temperature Θ in °C and frequency f into consideration. The coefficient 8.68 is to convert from Nepers to dB. Figure 1.3 shows α_w over a temperature range of 10°C - 30°C ([4] does not give this range, so it is extrapolated for average water temperatures). The attenuation term $10^{-\frac{2\alpha_w(R-R_0)}{10}}$ is plotted over range figure 1.4 at $\Theta = 14^\circ\text{C}$ for the

transducer frequencies. It shows that, at the working range, the attenuation term from water is negligible.

$$\alpha_w(f, \Theta) = 8.68 \cdot (2.1 \cdot 10^{-10}(\Theta - 38)^2 + 1.3 \cdot 10^{-7}) \cdot f^2 \quad [\text{dB m}^{-1}] \quad (1.33)$$

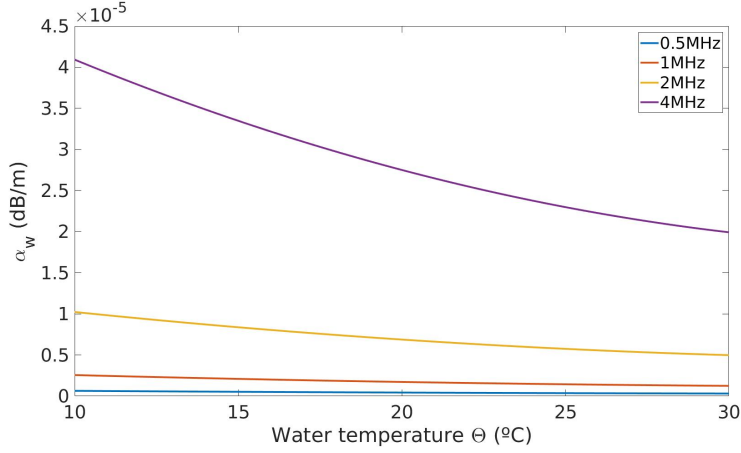


Figure 1.3: Attenuation coefficient α_w over water temperature Θ from [4]

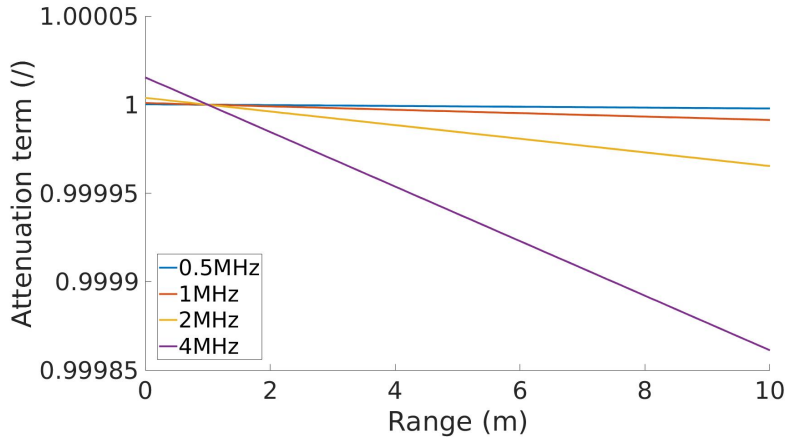


Figure 1.4: Attenuation term from water over range for 4 frequencies at $\Theta = 14^\circ\text{C}$

1.3.2 Bubbles attenuation

It is stated in [2, p. 314] that the attenuation from a bubbly medium can be written as

$$10^{-\frac{2\alpha_b(R-R_0)}{10}}$$

where coefficient α_b depends on the bubbly medium characteristics, such as bubbles radius distribution. In order to obtain this equation, [2] supposes in its equation (8.3.12) that $\sigma_e N$ does not depend on x (where N and x are notations from [2], corresponding to n and R). This independence from range cannot be assumed in the current case, so the equation has to be adapted. Let be $I_s(r)$ the incident wave intensity at range r . The power attenuation equation

can be written ([2]) as

$$\frac{dI_s(r)}{dr} = -I_0 S_e(r) \quad (1.34)$$

where $I_0 = I_s(R_0)$. S_e is the extinction cross-section per unit volume, defined further in chapter 5. Integrating, this leads to

$$I_s(R) = I_0 \exp\left(-\int_{R_0}^R S_e(r) dr\right) \quad (1.35)$$

which can be expressed in terms of pressure as

$$P_s(R) = P_0 \exp\left(-\frac{1}{2} \int_{R_0}^R S_e(r) dr\right) \quad (1.36)$$

Let be $B_t(R) = \int_{R_0}^R S_e(r) dr$. In terms of decibels,

$$\begin{aligned} P_s(R) &= P_0 10^{-\frac{10}{2 \ln 10} B_t} \\ &= P_0 10^{-2.17 B_t} \\ &= P_0 10^{-\frac{4.34}{20} B_t} \end{aligned} \quad (1.37)$$

The last expression allows to make factor 4.34 from [2] appears. If S_e is constant over the working range (as assumed in [2]), the same result as the one in the book is found.

Moreover, in chapter 6 is detailed another theory from [5] for attenuation. The script [attenuationScript.m](#) allows to compare results from the two theories.

Chapter 2

Directivity, beamwidth and insonified volume

This chapter deals with directivity, beamwidth, integrated beam-pattern, insonified volume and resolution considerations. Matlab script: [directivity.m](#).

2.1 Directivity and beamwidth

According to [2], the pressure directivity pattern $D_t(\theta)$ for a circular piston transducer of frequency f and radius A_t holds the following equation 2.1:

$$D_t(\theta) = \frac{2J_1(kA_t \sin \theta)}{kA_t \sin \theta} \quad (2.1)$$

where J_1 is the first order Bessel function, $k = \frac{2\pi f}{c}$ is the wave number and c is the sound speed in the water. The circular piston transducer model is used by AQUAtec for its transducers¹. The theoretical directivity patterns are plotted on figure 2.1 for the frequencies of the device: 0.5, 1, 2 and 4 MHz. From the directivity pattern can be theoretically computed the -3 dB two-ways directivity beamwidth D_t^2 for each frequency. Table 2.1 shows the corresponding theoretical values and the data provided by AQUAtec (the relative difference is less than 1.9 %).

Frequency f [MHz]	Two-ways -3 dB beamwidth [°]	
	according to AQUAtec	according to [2]
0.5	7.50	7.36
1	5	4.91
2	4.68	4.60
4	2.32	2.28

Table 2.1: Two-ways -3 dB beamwidths

¹Going through different papers, it seems the condition $kA_t \gg \pi$ has to be fulfilled, or something close to. An e-mail from AQUAtec support service states that the two ways -3 dB beamwidth should be greater than $\frac{30\pi}{kA_t}$. No real information found.

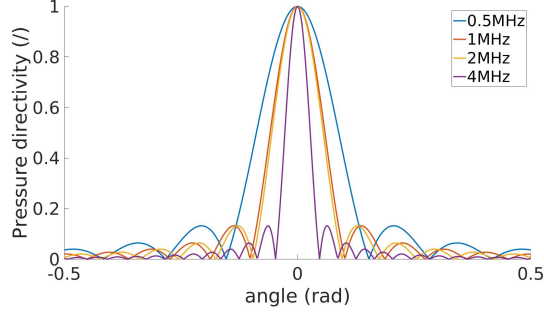


Figure 2.1: Theoretical directivity pattern D_t for the ABS transducers according to [2]

2.2 Integrated beam pattern

The integrated beam pattern ψ is defined in [2] as

$$\psi = \iint_{\theta, \phi} D_t^2(\theta, \phi) D_r^2(\theta, \phi) \sin \theta \, d\theta d\phi \quad (2.2)$$

In our case, the directivity patterns of the source and the receiver are considered the same and independent from ϕ , so it leads to equation 2.3. Table 2.2 shows the numerical results for the device.

$$\begin{aligned} \psi &= \iint_{\theta, \phi} \left(\frac{2J_1(kA_t \sin \theta)}{kA_t \sin \theta} \right)^4 \sin \theta \, d\theta d\phi \\ &\approx \frac{5.78}{(kA_t)^2} \quad \text{when} \quad kA_t > 10 \quad (\text{see [2, p. 360]}) \end{aligned} \quad (2.3)$$

Frequency f [MHz]	Integrated beam pattern ψ [sr]
0.5	0.0092
1	0.0041
2	0.0036
4	0.0009

Table 2.2: Integrated beam pattern values

In section 1.1 is made the assumption that $D_t^4(\theta)$ can be seen as a window:

$$D_t^4(\theta) = \begin{cases} 1 & \text{if } 0 < \theta < \theta_{mx} \\ 0 & \text{if } \theta_{mx} < \theta < \frac{\pi}{2} \end{cases} \quad (2.4)$$

If this assumption is used with equation 2.2 as proposed in **hypothesis 2**, it leads to

$$\begin{aligned}\psi &= \int_{\phi=0}^{2\pi} \int_{\theta=0}^{\theta_{mx}} \sin \theta \, d\theta d\phi \\ \Rightarrow \theta_{mx} &= \arccos\left(1 - \frac{\psi}{2\pi}\right)\end{aligned}\tag{2.5}$$

2.3 Insonified volume and resolution

In this section is explained the integral limits $R \pm \frac{L}{2}$ of equation 1.11.

Let L be the resolution length of the device: an object in a range between $R - \frac{L}{2}$ and $R + \frac{L}{2}$ will be considered as being at range R . The transducer works by sending a sound wave of duration τ , and c is the sound speed in water. For one wave, the device starts emitting at t_0 and stops at $t_0 + \tau$. At t_R and t_{R+L} , the device receives the fronts of the signal backscattered from ranges R and $R + L$ respectively. The two signals will overlap if $\Delta t = t_{R+L} - t_R < \tau$. The limit is then for $\Delta t = \tau$. It comes the following equations:

$$\left. \begin{aligned}t_R &= \frac{2R}{c} \\ t_{R+L} &= \frac{2(R+L)}{c}\end{aligned} \right\} \Rightarrow \Delta t = \frac{2L}{c} \left. \begin{aligned} & \\ \Delta t &= \tau \end{aligned} \right\} L = \frac{\tau c}{2}\tag{2.6}$$

For $L = \frac{\tau c}{2}$, the device can make the difference between two scattering objects at ranges $R - \frac{L}{2}$ and $R + \frac{L}{2}$. If the range distance between them is shorter than L , the objects cannot be isolated. The parameter L is called bin size, or resolution.

Figure 2.2 illustrates the insonified volume, defined in equation 1.25.

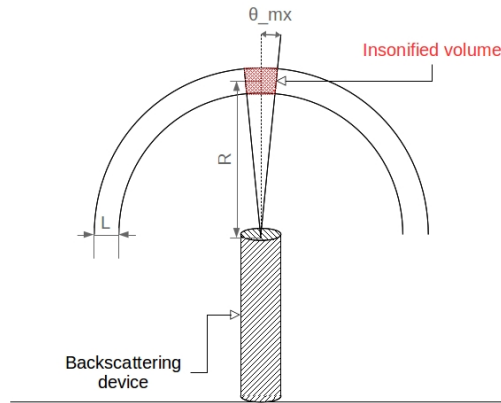


Figure 2.2: Insonified volume illustration

Chapter 3

Extracting data from the device

This chapter deals with getting information from raw data. The device is presented, as well as the raw data. A calibration theory is also proposed, but it does not fit accurately the experimental result. Further work must be carried out (see section 3.4).

Matlab script: [plotData_3D.m](#).

AQUAtec supplies a software to extract data from the device and to convert the files format. In our case, the software could not be installed, so a Matlab script from AQUAtec has been adapted for this purpose (in a shorter time than AQUAtec): see [exportConvertABS.m](#).

3.1 Device short presentation

The device is an AQUA*scat* 1000S. It aims to measure sediment concentration by using acoustic backscatter method. Four transducers are available on the device, and their characteristics are shown in table 3.1.

NOTE *ABS data also give the transducers radius, however radius for 0.5 MHz is wrong (given 9 mm, real 12 mm). More, data are sorted according to [1, 2, 4, 0.5] MHz, which is not convenient. For logical purpose, I usually sort according to increasing frequency, especially in function [loadABS_Data.m](#).*

Frequency f [MHz]	Radius A_t [mm]
0.5	12
1	9
2	4.8
4	4.9

Table 3.1: Transducers characteristics from AQUAtec

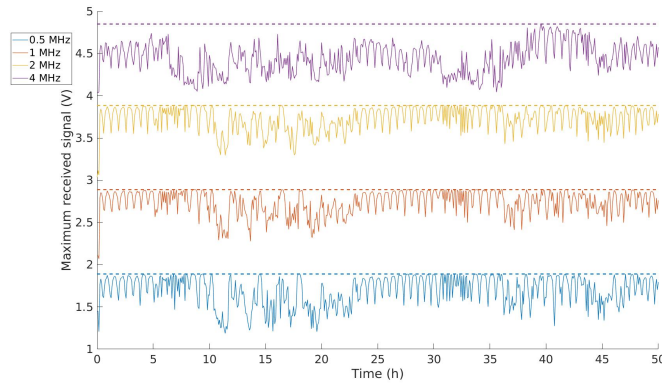


Figure 3.1: IPMA 2016 data - Signal received from surface
(The signals are shifted up (+1))

3.2 IPMA set of data

In [6, chapt. 5] is presented a set of backscattering data from 2016 that, in the current document, are used to test the Matlab scripts and the methods. The signal was recorded every 5 minutes during 2 diurnal periods with a bin size of 40 mm. Below are presented some considerations about these data:

- A periodical pattern can be seen in the signal received from surface range
- The 4 MHz quality of the signal needs to be verified, as it looks rather poor on the whole
- The raw signal is range compensated

3.2.1 About the periodical pattern

Figure 3.1 shows the signals for the 4 frequencies received from surface range. A periodical pattern can be seen, in 0-5 h or 25-30 h. The period is 40 min. This figure as been plotted by choosing the maximum value of the raw signal. The periodical pattern can be explained with the tide height and the resolution. The tide decreases in 0-5 h at 0.05 m/h, which means it needs 48 min to fall 40 mm down (bin size). The 40 minutes period is of the same order. Figure 3.2 shows the signal between 2 and 5 h: the tide height can be seen moving down, and due to integration procedure, the backscattering signal is either in one bin or astride two bins.

NOTE *Integration of the signal around the surface range does not solve the problem (tried in `plotData_3D.m`): There is no linearity (adding two bins does not lead to one bin). Control with equation 1.30, compensation taken into account.*

A periodical pattern should also appear when the tide is increasing. It is not the case, because the tide increases faster, and the bin size is too broad, which acts as a filter.

3.2.2 About the compensation

Figure 3.3 shows the raw data extracted from the device for the whole experiment, at 1 MHz (signals for the other frequencies are the same). The surface is clearly visible (yellow line). Two

datatips show the value of backscattered signal received from the surface at low and high tide, in dB (chosen at maximum received signal on the periodical pattern of previous subsection). Let be assumed that:

- The surface is a perfect mirror (see 3.4),
- The energy loss due to bubbles is negligible on the way,
- The raw signal is $v_r(R)$ with notations of chapter 1.

Under these assumptions, the signal must be, at least, subject to spherical attenuation R^{-1} (see equation 1.28). Table 3.2 shows the values of received signal, and the ones predicted by the theory. It can clearly be seen that there is no spherical decrease in raw data. It can be explained by a pre-compensation for range from AQUAtec software (not stated in the technical documents). The raw data is not v_r but $v_r \times R$. If the data are "decompensated" from range (i.e divided by R), the same process than previously leads to second part of table 3.2. In that case, the differences match, which proves the range R compensation.

Hypothesis on raw data	Range (m)	Time (h)	Raw signal level (dB)	Difference (dB)	Theoretical difference (dB)
$= v_r$	0.96	30.08	-0.5166	0.0197	4.65
	1.64	8	-0.5363		
$= v_r \times R$	0.96	30.08	-0.3396	2.346	2.326
	1.64	8	-2.685		

Table 3.2: Signal level difference: raw data vs. theory, $f = 1$ MHz

3.3 Rewriting the equations

The laboratory does not have the proper equipment to make a complete characterization of the device. The following method is adapted from [2] and [7]. Let us start by writing equation 1.30 slightly differently. The frequency dependency f is written back.

$$\begin{aligned}
 v_r^2(f, R) &= v_s^2(f) K_r^2(f) G_s^2(f) \frac{R_0^2}{R^2} \frac{M_v(f, R)}{4\pi} \psi(f) L 10^{-2 \cdot att(f, R)} \\
 &= C_0^2(f) \frac{M_v(f, R)}{R^2} 10^{-2 \cdot att(f, R)}
 \end{aligned} \tag{3.1}$$

where

$$C_0^2(f) = v_s^2(f) H_{sr}^2(f) \frac{R_0^2}{4\pi} \psi(f) L \tag{3.2}$$

$$H_{sr}(f) = K_r(f) G_s(f)$$

In theory, for a specified set of parameters (f, L), the value of C_0^2 is constant and does not vary with range R . By using the auto-calibration method described below, one can access this value.

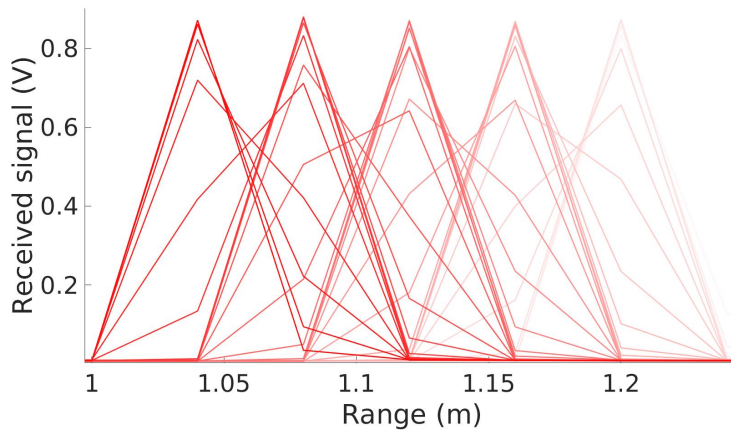


Figure 3.2: IPMA 2016 data - Signal received (focused on surface range)
 Time evolution between 2 h (white) and 5 h (red) after the experiment starts, for 1 MHz

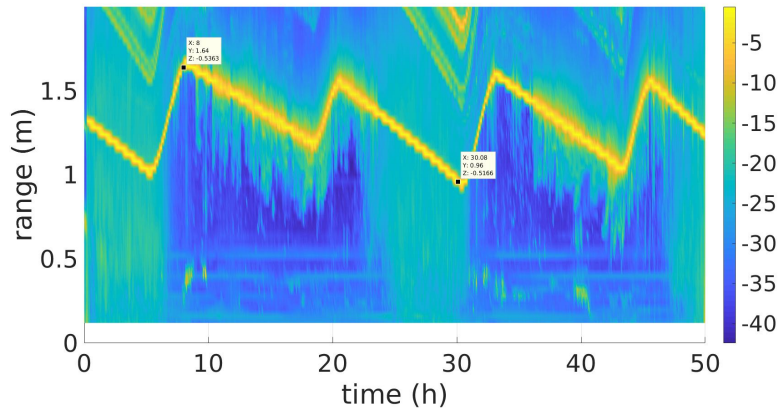


Figure 3.3: IPMA 2016 data - Raw signal for 1 MHz

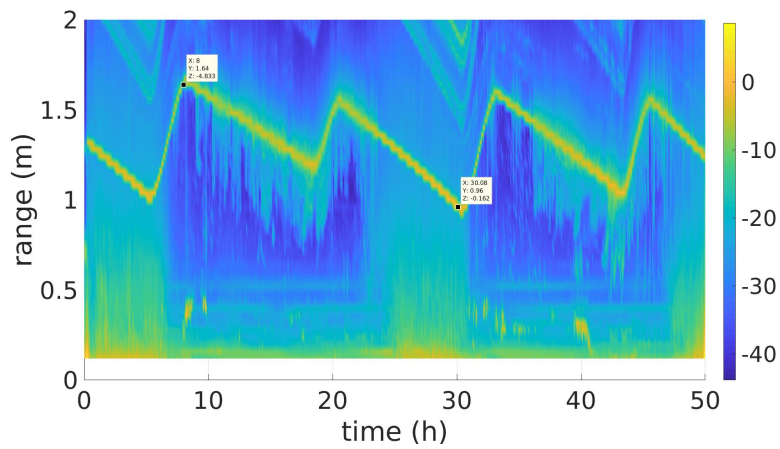


Figure 3.4: IPMA 2016 data - "Decompensated" signal for 1 MHz

3.4 Auto-calibration method

This method is adapted from [2]. Figure 3.5 illustrates the setup¹. The idea is to calibrate the device by pointing it toward a smooth water/air interface in a water tank. This surface is assumed to be a large enough perfect mirror. The distance $R = R_{ref}$ is measured and from the perfect mirror assumption, $|L_s(R_{ref})| = 1$ in the insonified volume $V_{ins}(R_{ref})$ (see chapter 1), which leads to

$$\begin{aligned} M_v(f, R_{ref})V_{ins}(R_{ref}) &= 4\pi \Delta\sigma_{BS} \\ &= 4\pi \end{aligned} \tag{3.3}$$

and then

$$\begin{aligned} M_v(f, R_{ref}) &= \frac{4\pi}{V_{ins}(R_{ref})} \\ &= \frac{2}{LR_{ref}^2 \left(1 - \sqrt{1 - \frac{9}{(kA_t)^2}}\right)} \end{aligned} \tag{3.4}$$

Another strong assumption is done for the calibration experiment: the bubbles in water are negligible, so that the attenuation term from bubbles (see chapter 5) is equal to 1. Since the water attenuation is also negligible, it is then possible to calculate $C_0^2(f, L)$ as

$$C_0^2(f, L) = \frac{v_{r,ref}^2(f)}{4\pi} R_{ref}^2 V_{ins}(R_{ref}) \tag{3.5}$$

Again, this value is supposed to be constant for a fixed frequency. However, making multiple measurements at different range will allow to validate this. If the value is not constant with range, then multiple measures will have to be conducted.

As stated in introduction, this section needs corrections and experimental validation to properly calibrate the device. The biggest issue lies in the wave model used under perfect-mirror assumption: [2] assumes plane wave propagation, so that doubling the distance leads to doubling the propagation attenuation, which is really different from spherical wave propagation. More, how the insonified volume relates to the interface still poses a challenge.

¹Please note the device height parameter h_d is different from the length of the device and takes into account the anchoring structure (not shown in figure 3.5).

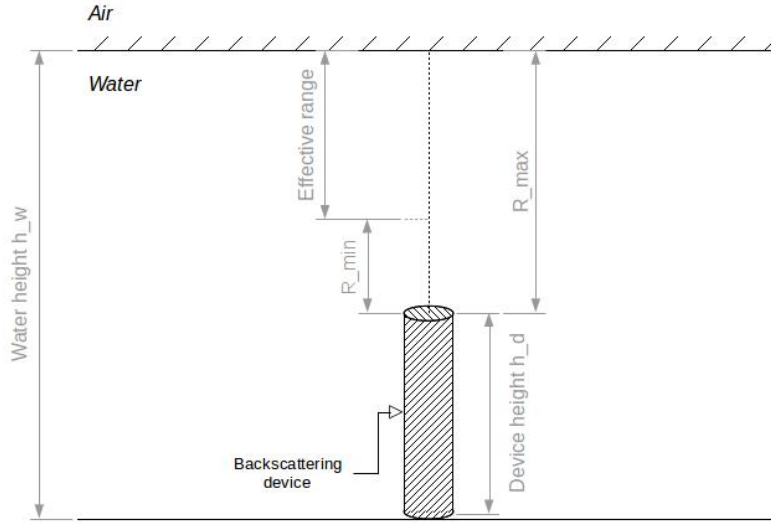


Figure 3.5: Calibration setup
The device is on the ground and points toward the air/water interface

Parameter	Unit	Symbol	Transducer direct setting	Comment
Water height (from tank bottom)	m	h_w	No	Max 1.60
Device height (from tank bottom)	m	h_d	No	Structure included
Transducer frequency	MHz	f	No	0.5, 1, 2 and 4
Maximum range (from transducers)	m	R_{max}	No	
Minimum range (from transducers)	m	R_{min}	No	
Effective measured range	m	ΔR_{eff}	No	
Bin size	mm	L	Yes	2.5, 5, 10, 20 or 40
Number of bins	/	N	Yes	From 1 to 256
Start bin	/	N_0	Yes	
Transmit power	dB	T_x^{dB}	Yes	0, -6, -12 or <i>off</i>
Gain relative to default	dB	R_x^{dB}	Yes	0, +12 or +20
Profile rate	Hz	f_{prof}	Yes	From 1 to 128
Profile length	s	τ	No	
Burst length	s	T_{burst}	No	
Burst interval	s	T_{int}	Yes	
Number of stored profiles	/	m_{prof}	Yes	To average in post-treatment

Table 3.3: Parameters to be set for the calibration experiment

Table 3.3 shows the parameters that should be set for each calibration test. Each frequency must be tested independently. The water height can be set in the tank, allowing it to be adjusted

as needed, up to 1.60 m. Noise measurement should also be performed, by recording without sending power, and at each water level. With the notations from this table, the following equation holds (with c the sound speed in water):

$$\begin{aligned}
L &= \frac{\tau c}{2} & \Delta R_{eff} &= R_{max} - R_{min} \\
R_{min} &= N_0 \times L & T_{burst} &= \frac{m_{prof}}{f_{prof}} \\
R_{max} &= (N - N_0) \times L & T_{int} &\geq T_{burst}
\end{aligned} \tag{3.6}$$

Regarding the geometry parameters, the device is 51 cm high, the large structure is 34 cm high and the fixing tool is 44 cm high. Taking into account the space needed by the cables, the top of the device should not be higher than 60 cm from the tank ground, in order to be able to have the water/air interface at $R_{max} = R_0 = 1$ m. To adjust near range equations (see section 3.6) with experiment, it can be interesting to record data close to the transducers.

3.5 Accessing the backscattering cross-section per volum unit

Informations are in $M_v(f, R) \times 10^{-2att(f,R)}$. Once the calibration has been conducted for each frequency f available on the ABS, i.e $C_0^2(f, L)$ is known, it is easy to access the product:

$$\begin{aligned}
v_r^2(f, R) &= C_0^2(f) \frac{M_v(f, R)}{R^2} 10^{-2 \cdot att(f,R)} \\
\Rightarrow M_v(f, R) \times 10^{-2att(f,R)} &= \frac{R^2}{C_0^2(f)} v_r^2(f, R)
\end{aligned} \tag{3.7}$$

3.6 About near field correction

It has been shown in [8] that, for the backscattering signal level in a range near from the transducer, “there is a significant departure from the spherical spreading response”. The document proposes a backscatter expression (that is the one used by AQUAtec device) and a near field correction factor ξ (that is not used by AQUAtec *as it is*) that are both described in Appendix.

Even though these equations are not used here, the near range effect can be taken into consideration by considering the previous equations only far from the device (see figure 3.6). The 2 MHz transducer has the shortest near-range limit while the 4 MHz has the longest one. Figure 3.6 shows the ξ factor for the four transducers. For $\xi = 1.1$, the 2 MHz limitation is 7.5 cm and the 4 MHz limitation is 15.2 cm.

One should notice that near-range equation depends on both frequency and transducer radius. Since transducers radius are not constant on the device (see table 3.1), the results can differ from the expectation when taking only frequency into account. However, it will be seen later (chapter 4) that near range effect does not seem to follow the equation.

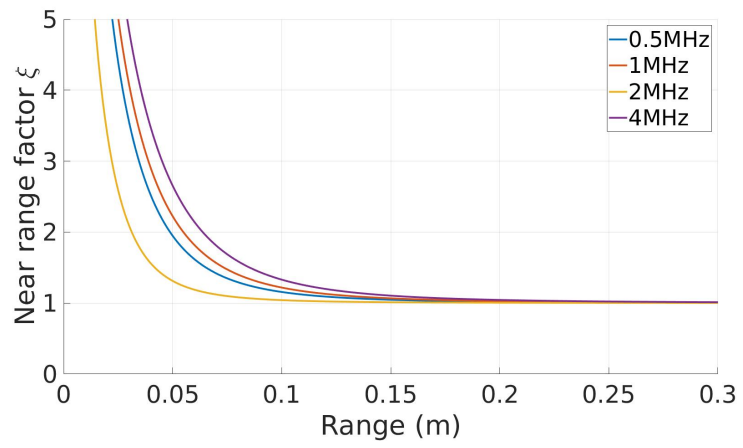


Figure 3.6: Near range factor ξ from [8]

Chapter 4

Calibration experiment

The following chapter reports the calibration experiment that has been carried out by Paulo FELISBERTO and Jef PHILIPPINE on 2018, February 15 in the water tank of the IPMA-EPPO (Estação Piloto de Piscicultura de Olhão), Olhão, in the framework of the SEAUX project. It first describes the tank location and the experimental setup, then presents the data and the associated processing. The methods proposed by AQUAtec in the software AQUAscat will not be used, regarding the equipment they need to be carried on. Matlab scripts: [calibration150218.m](#) and [loadABS_Calibration.m](#). The data are under Calibration_15022018 folder.

4.1 Overview of experimental setup

4.1.1 Tank location and device

The experimental area is located at the IPMA-EPPO Olhão. The chosen tank was empty at first (see pictures 4.1 and 4.2), allowing the equipment to be installed, then filled with water. During the experiment, the water level did not change and the water pumps were not working. The tank was not clean, and possible interferences from particles and floating grass could have taken place (see section 4.2.3). The device was powered by the AQUAscat battery pack and USB-linked to the computer, so that parameters could be directly set and test started.



Figure 4.1: Tank and working table



Figure 4.2: Device in the empty tank



Figure 4.3: Device in the tank (close view)

4.1.2 Parameters description

Figure 3.5 shows the setup notations used in the report. The geometrical¹ and fixed values are presented in table 4.1, and the variable parameters in table 4.2. As shown in 4.2, 18 sets of parameters were tested. Device and transducers are supposed completely perpendicular to the water surface. Water level has been measured by hand when installing the structure, and the transducers orthogonality (relating to the device itself) have not been tested.

Parameter	Unit	Symbol	Value
Water height (from tank bottom)	m	h_w	1.60
Device height (from tank bottom)	m	h_d	0.61
Maximum range (from transducers)	m	R_{max}	1
Profile rate	Hz	f_{prof}	40
Number of stored profiles	/	m_{prof}	6000
Burst length	s	T_{burst}	150

Table 4.1: Fixed parameters of the calibration experiment

Parameter	Unit	Symbol	Values		
Transmit power	dB	T_x^{dB}	<i>off</i> and 0		
Gain relative to default	dB	R_x^{dB}	0, +12 and +20		
Bin size	mm	L	2.5	10	40
Number of bins	/	N	256	256	30
Start bin	/	N_0	300	1	1
Minimum range (from transducers)	m	R_{min}	0.750	0.01	0.04
Effective measured range	m	ΔR_{eff}	0.640	2.56	1.20

Table 4.2: Parameters to be set for the calibration experiment

The transmit power T_x^{dB} was set *off* to carry out noise measurements². The water temperature Θ was measured for every set and was 14.7°C for the 7 first trials and 14.9°C for the others. It is used to correct the sound speed water c in the tank (1500 m s^{-1} in the device

¹Please note the device height parameter h_d is different from the device length and takes into account the anchoring structure (not shown in figure 3.5).

²*off* actually means -18,06 dB

software), according to equation 4.1 (from [2]). The temperature is fixed at $\Theta = 14.8^\circ\text{C}$ in the data analysis, so it leads to $c = 1505 \text{ m s}^{-1}$.

$$c = 1449.2 + 4.6 \Theta - 0.055 \Theta^2 \quad (4.1)$$

The salinity is not taken into consideration (almost 35 ppm in the tank).

4.2 Experimental data

Figures 4.4 to 4.9 show the recorded raw data. Different setups are tested, presented in table 4.2. Each figure shows either noise or “signal” data, (respectively transmit power $T_x^{dB} = 0$ or off), for a specific resolution L and gain relative to default R_x^{dB} .

4.2.1 First remarks

Several remarks can be done:

- The effective measured range ΔR_{eff} for $L = 10 \text{ mm}$ was too broad (see figure 4.7). It should have been focused on the surface range, as with $L = 2.5 \text{ mm}$ (see figure 4.5). Near range effects and echoes (signal from 2 m) are visible. It does not really matter since manual processing is performed afterwards.
- The near range effect is clearly visible when $L = 10 \text{ mm}$ (see figure 4.7). Due to resolution issues, this effect is visible only for $f = 0.5 \text{ MHz}$ when $L = 40 \text{ mm}$ (see figure 4.9). However, the results do not match the theory presented in chapter 2: for instance, the signal for $f = 4 \text{ MHz}$ should have the longest near range value, but in this case the signal for $f = 0.5 \text{ MHz}$ clearly has it. Awaiting possible further measurements, 20 cm should be considered as the near range limit for the 4 frequencies.
- The gain relative to default R_x^{dB} effect is difficult to properly understand. Figure 4.10 shows the signal for $L = 2.5 \text{ mm}$, focused on surface range. The full scale does not change (almost 1 V), and the gain seems to be applied only on low level. In [calibration150218.m](#) are calculated the R_x^{dB} values for all signals from figures 4.4 to 4.9, and these values are not what they are supposed to. Range compensation has already been detailed (see section 3.2.2): I wonder if the device applies some kind of non-linear gains on the data.
- 40 mm resolution is too wide for such an experiment (see figure 4.11 for the signal focused on the surface range). In [6], the tide of the tank (directly connected to Ria Formosa) is said to be varying around 1.80 m. The device height was by then 74 cm, the minimum level from the device top was about 1 m and the maximum level about 1.5 m, so a tide of 50 cm. It leads to a minimum tide from the ground of about 1.80 m and a maximum tide about 2.30 m. Table 4.3 shows the maximum effective measured range according to the bin size. A 2.5 mm resolution is not enough to cover the whole range, even with the device height. A 5 mm resolution (also possible, even though not tested here) would allow $\Delta R_{eff} = 1.28 \text{ m}$. Adding the 20 cm near range limit and the necessary device height h_d (minimum 60 cm), the whole range between the device and the high tide level is almost covered. The other resolutions would lead to a wider and useless covered range. Of course, this is a trade off between range and resolution.

- Strong signature is received from above the water surface and is difficult to explain. The first idea was relating to the spherical insonified volume (see figure 2.2): signal from the outside limits ($\theta = \theta_{mx}$) should arrive later than signal from the center ($\theta = 0$), but basic geometrical calculations do not lead to the right equivalent range value. [3, p.634] states that such a signal is “due to surface reverberation”, but does not deal any further with this matter. The experiment described in [3] takes place offshore, where waves and wind conditions seem to have important impact. It is hard to estimate the impact of such conditions for the present experiment, since it took place in a small tank, protected from waves and wind. This question is still unanswered and might play a part in the proper calibration of the device.

L (mm)	ΔR_{eff} max (m)
2.5	0.640
5	1.280
10	2.56
20	5.120
40	10.240

Table 4.3: Maximum effective measured range according to resolution

4.2.2 Signal to noise ratio

A signal to noise ratio is computed to estimate the impact of noise on the measurements. The signal energy is calculated as shown in equation 4.2. The near range effect is not taken into consideration for this ratio, so the integration ranges for $L = 10$ mm and $L = 40$ mm are respectively [0.2 m ; 1.9 m] and [0.2 m ; 1.2 m]. For $L = 2.5$ mm, the whole signal is integrated. The signal to noise ratio SNR is then calculated in equation 4.3 and the results are shown in table 4.4 when $R_x^{dB} = 0$ dB. The ratio is high enough for the noise to be neglected.

$$E(v_r) = \sum_R v_r^2(R) \quad (4.2)$$

$$SNR = \frac{E(v_r(signal))}{E(v_r(noise))} \quad (4.3)$$

$R_x^{dB} = 0$ dB		Frequency (MHz)			
		0.5	1	2	4
L (mm)	2.5	33	33	44	46
	10	47	55	58	54
	40	48	45	63	67

Table 4.4: Signal to noise ratio (in dB) for $R_x^{dB} = 0$ dB

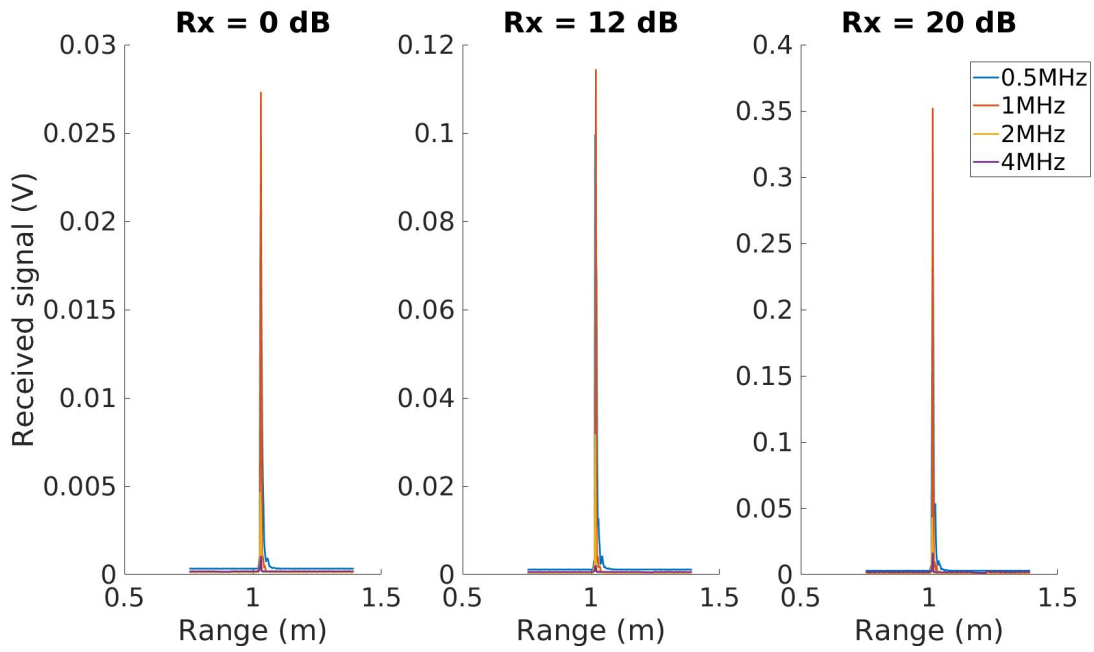


Figure 4.4: Noise for $L = 2.5$ mm

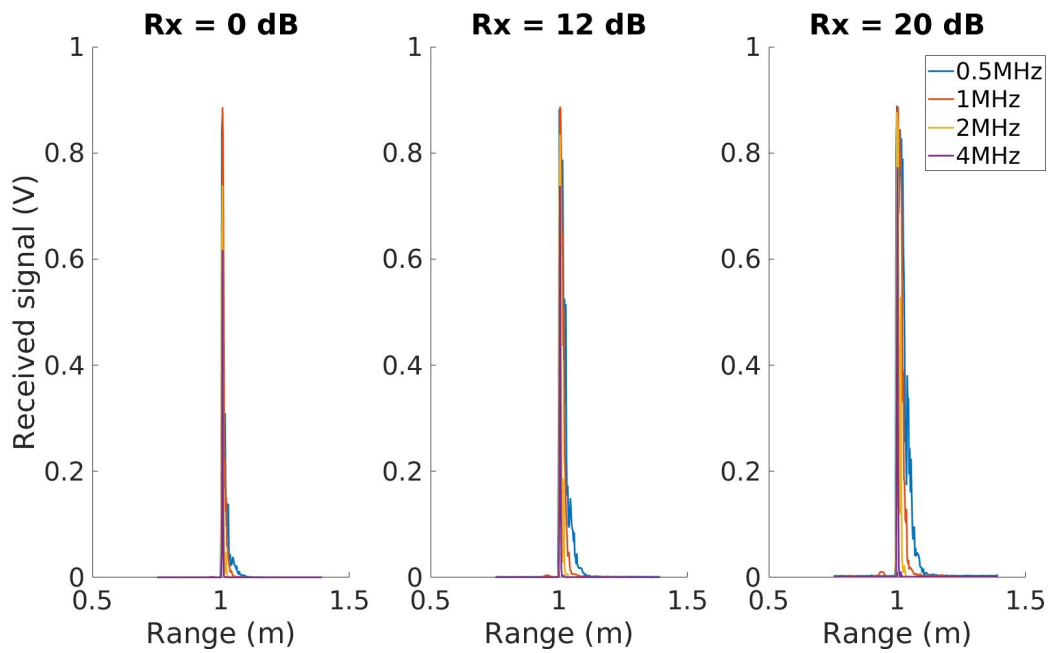


Figure 4.5: Signal for $L = 2.5$ mm

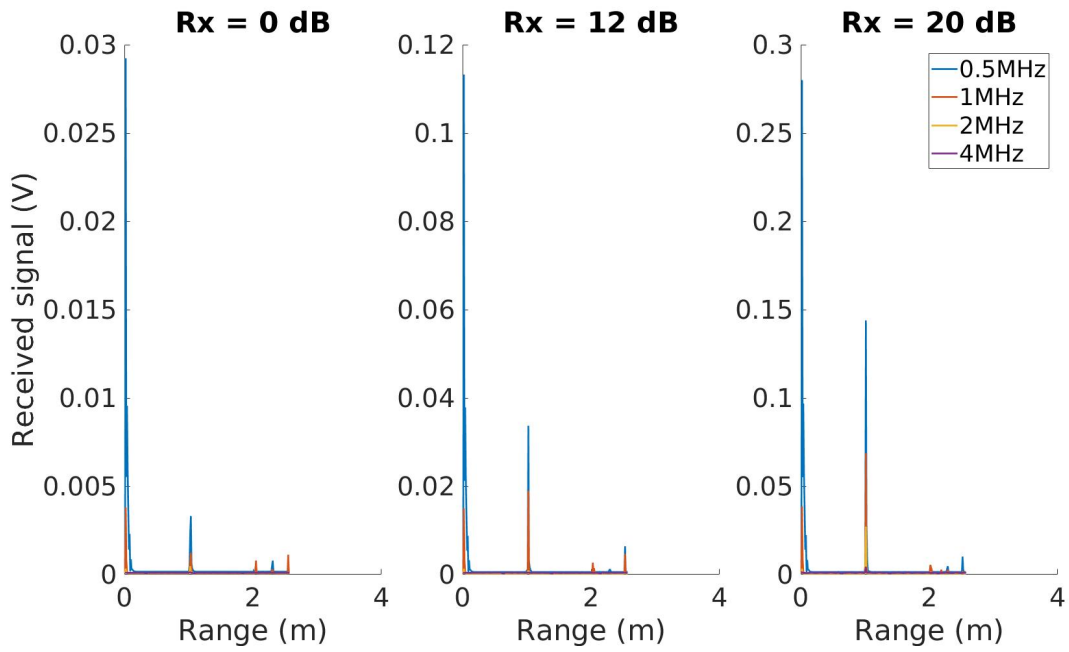


Figure 4.6: Noise for $L = 10 \text{ mm}$

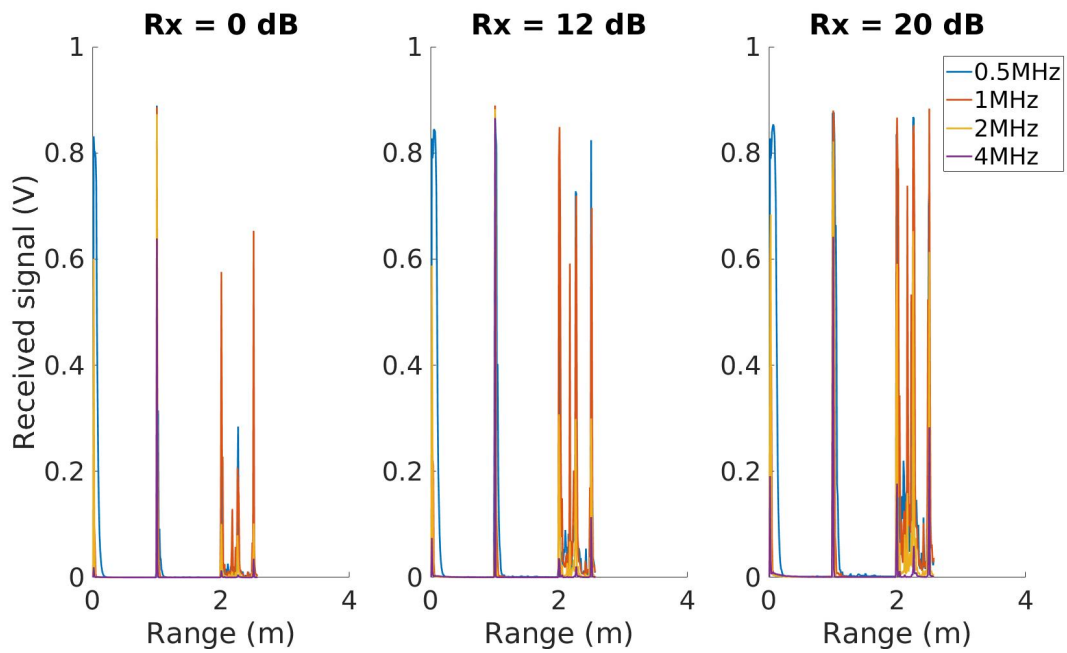


Figure 4.7: Signal for $L = 10 \text{ mm}$

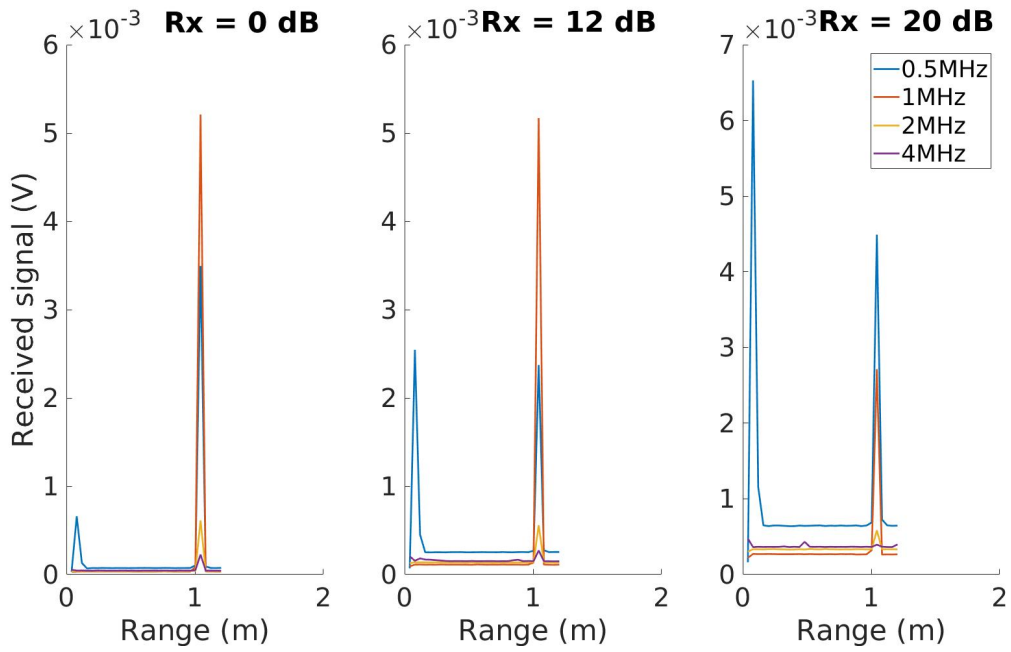


Figure 4.8: Noise for $L = 40\text{ mm}$

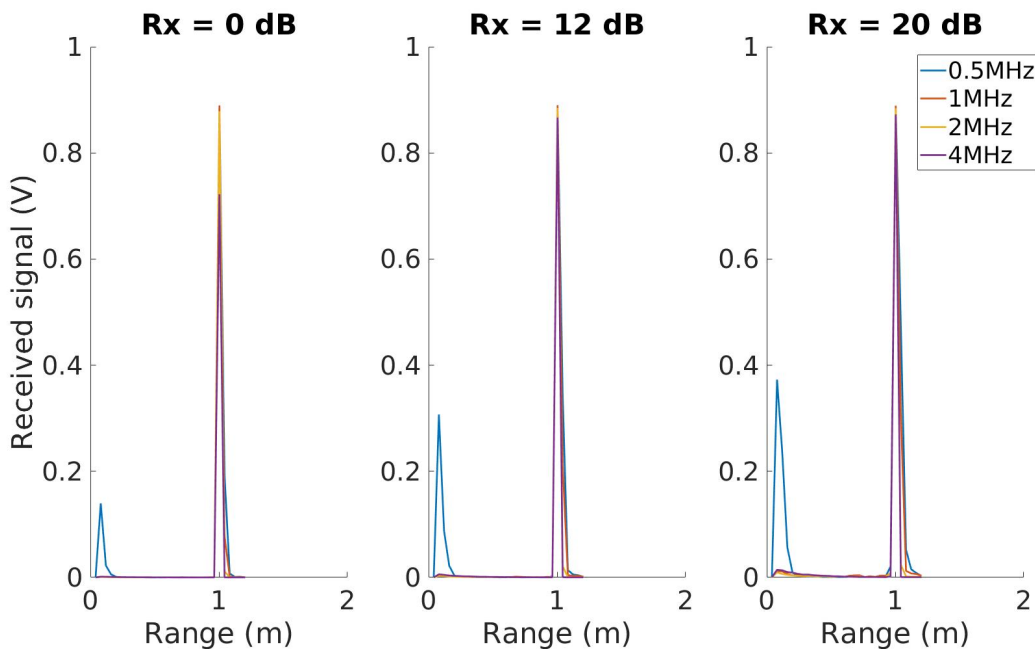


Figure 4.9: Signal for $L = 40\text{ mm}$

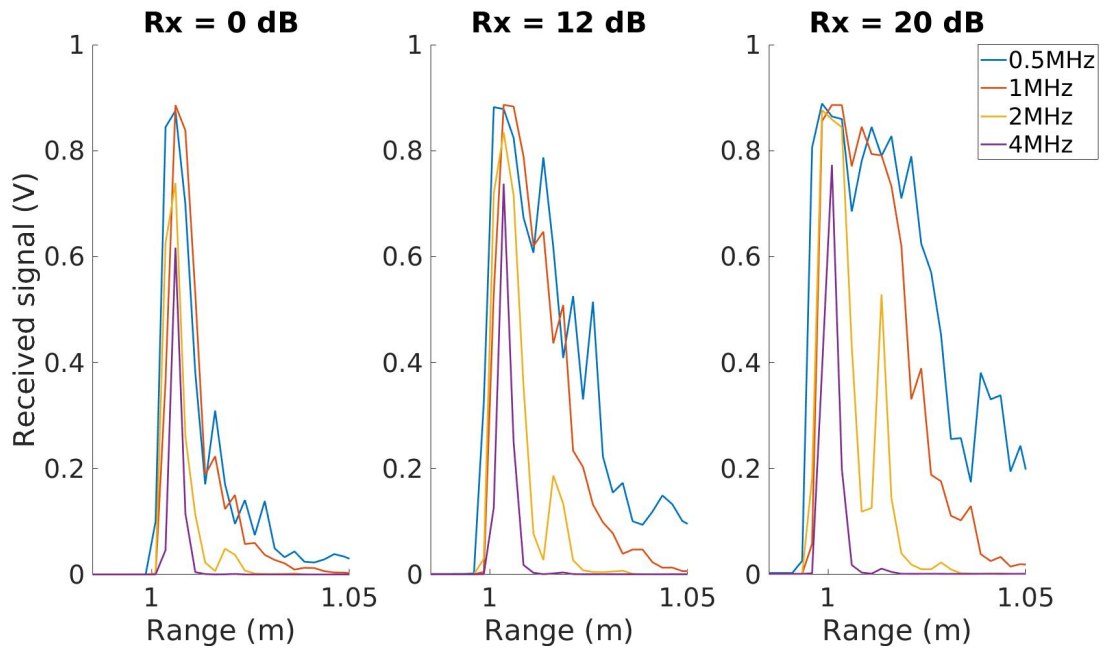


Figure 4.10: Signal for $L = 2.5$ mm (focus on surface range)

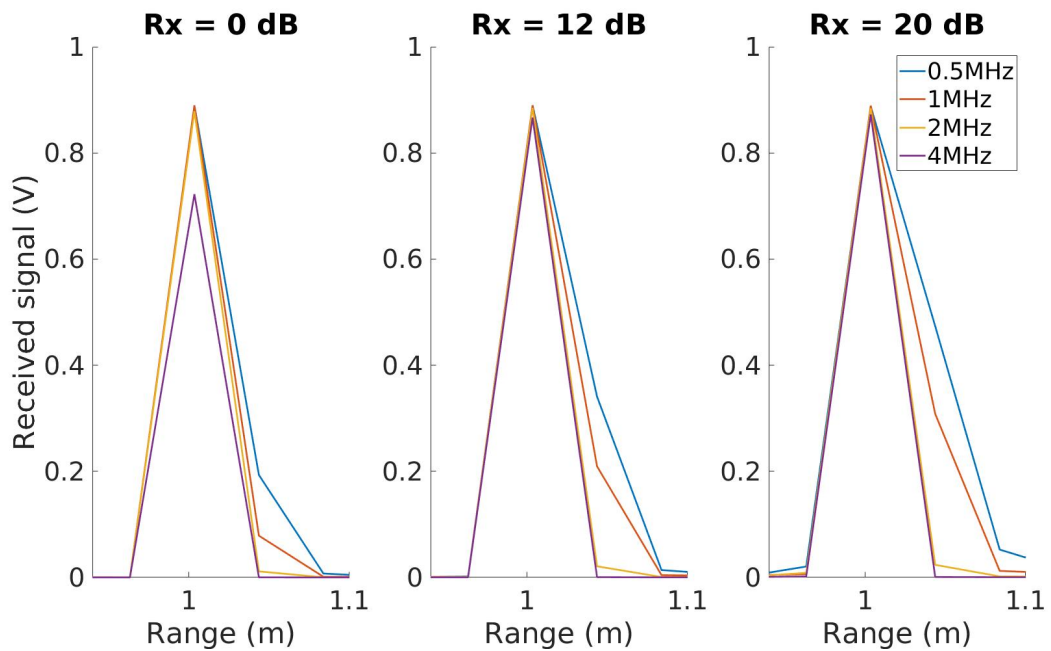


Figure 4.11: Signal for $L = 40$ mm (focus on surface range)

4.2.3 About particles in the water

Figures 4.12 and 4.13 show the logarithmic signals for $L = 2.5$ mm and $L = 10$ mm, both focused on surface range. For $L = 2.5$ mm, two peaks (at $R = 0.84$ m and $R = 0.96$ m) are clearly visible for $f = 1$ MHz, independently from the values of R_x^{dB} , and can also be seen for $L = 10$ mm. These peaks could be symptomatic of some unexpected material just below the water surface. The fact that only $f = 1$ MHz detects it could be (*this is only an idea and has not been verified yet*) related to scattering cross-section resonance with material radius (see figure 5.2).

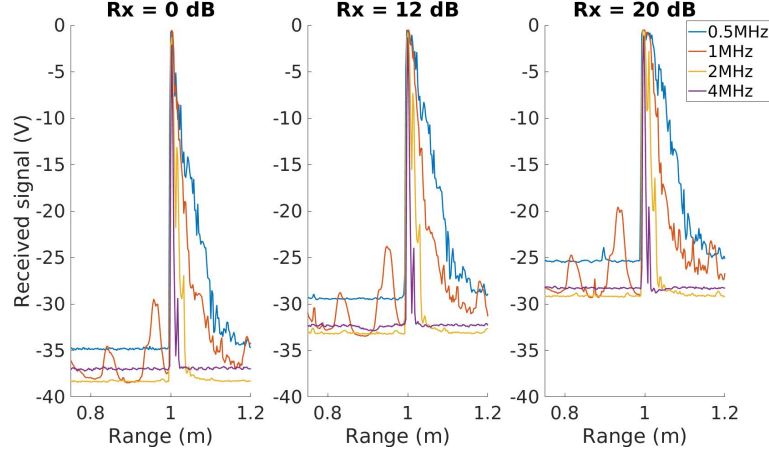


Figure 4.12: Signal (dB) for $L = 2.5$ mm (focus on surface range)

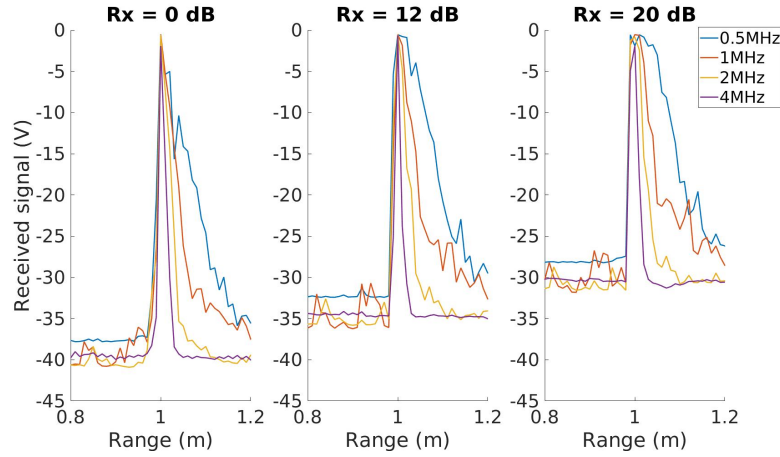


Figure 4.13: Signal (dB) for $L = 10$ mm (focus on surface range)

4.3 Processing the data

Equation 3.5 shows how to access the value of $C_0^2(f, L)$. Since the effect of parameter R_x^{dB} is for the moment unknown, only the signals for $R_x^{dB} = 0$ dB and $R_x^{dB} = +12$ dB are processed in [calibration150218.m](#)

4.4 Further calibration work

This chapter has presented the setup and the data of the experiment, as well as the calibration results. Here are some notes about the further work related to this calibration. In order to characterize near range effects and make the measurements for the 5 mm resolution, another experiment has been carried out at IPMA-EPPO, on Mai 21st 2018. Due to lack of time, the data could not be processed: only the conversion *.aqa to *.mat has been done. Below are the main parameters that have been chosen:

- The transmit power was set to 0 dB, -6 dB and -12 dB.
- The gain relative to default was set to 0 dB and 12 dB.
- The bins sizes were 2.5 mm and 5 mm.
- The number of bin was 256 for every measure.
- The tank was way cleaner than the first time.

We then theoretically have 12 files. However, it seems 2 are missing, for an unknown reason. The experiment has been carried out so that the post-treatment should be easier than the first one, especially because the data lengths are now all the same (256 bins). It means that loops and automatic processes can be used. It seems insignificant, but writing operations manually takes a lot of time!

Chapter 5

Backscattering cross-section distribution

This chapter deals with the backscattering cross-section, the bubble size distribution, and introduce the extinction cross-section. It is stated in [9] that several formulas exist for these cross-sections, depending on authors and hypothesis. This chapter shows the first formulations that have been chosen, then explains their limitations and indicates the final formulas.

Oxygen bubbles size depend mainly on water movement, and not on seagrass species: a weak water flow allows the bubble to grow on the leaf surface, so that large radius is reached when it comes off. On the contrary, strong water movements lead to small bubble radius. This fact can allow to make assumptions on bubbles size.

Matlab script: [crossSectionCalc.m](#).

5.1 Extinction cross-section

Closely related to backscattering cross-section per unit volum M_v , the extinction cross-section per unit volum S_e is actually the total cross-section of a particle, due simultaneously to backscattering and absorption. It represents the total losses of energy from the incident beam (see [2, chapt. 8]). As stated and explained in chapter 1, the attenuation term from bubbly medium can be written as

$$10^{-\frac{4.34}{20} \int_{R_0}^R S_e(r) dr} \quad (5.1)$$

Since the attenuation from water can be, at the working range of this paper and as shown in chapter 1, considered as negligible, the attenuation term at range R is due to bubbly water only:

$$att(R) = \frac{4.34}{20} \int_{R_0}^R S_e(r) dr \quad (5.2)$$

Related to the extinction cross-section per unit volume S_e , the extinction cross-section σ_e is defined as the equivalent of σ_{BS} for M_v (see equation 1.7).

5.2 How to isolate M_v and $10^{-2 \cdot att}$

As stated in chapter 3, the product $M_v(f, R) \times 10^{-2att(f, R)}$ can be extracted from the device. From this product, we must isolate M_v and 10^{-2att} . An iterative method is proposed in [3], roughly explained below. Two difficulties are encountered: first, isolate backscattered signal from bubbles attenuation (the main issue here). Second, closely related (we deal with it in section 5.6), the way to extract n from M_v and S_e is not petty. In the following method, we assume a way is known to extract n .

“Bottom-up” strategy: The idea is to start from the first bin (the closest from the device), considering the attenuation term 10^{-2att} is negligible for such a short distance (also considering there are no bubbles at the top of the device). The initial value is then M_v . The computation starts from the bottom to reach the furthest bin.

Initialisation First bin: 10^{-2att} is assumed equal to 1. M_v value is immediate. n can be computed.

Iteration For a specific bin:

1. 10^{-2att} is calculated from n value of previous bin.
2. M_v value is immediate, so n can be computed.
3. Next step.

Another iterative method (that could be called “top-down”) could be used. Under the assumption that total attenuation along the way (i.e attenuation of the last bin) is known, then the same process from previous method can be applied. With figure 5.7 (see theory below), one can also notice that M_v and S_e can be assimilated for large enough bubble radius. Under such an assumption, the calculation can be made easier.

5.3 Bubble size distribution

It is stated in [2, p. 310] that, when ”widely spaced bubbles are insonified, the acoustical cross-section of the individuals simply add”. It is assumed right in this report without discussion. For a given bubble size distribution $m(a, R)$ in the insonified volume $V_{ins}(R)$ defined in chapter 1, and with σ_{BS}, σ_e the backscattering and extinction cross-section respectively (σ_e is to S_e what σ_{BS} is to M_v), it can be written

$$\sigma_{BS}(R) = \sum_a m(a, R) \sigma_{BS}(a, R) \quad (5.3)$$

$$\sigma_e(R) = \sum_a m(a, R) \sigma_e(a, R) \quad (5.4)$$

where the a dependency denotes the parameters for only one bubble radius. The backscattering cross-section per volume unit $M_v(f, R)$ and the extinction cross-section per volume unit $S_e(f, R)$

over the insonified volume at range R can then be written as

$$\begin{aligned} M_v(f, R) &= \frac{1}{V_{ins}(R)} \sum_a m(a, R) \sigma_{BS}(a, f, R) \\ &= \sum_a n(a, R) \sigma_{BS}(a, f, R) \end{aligned} \quad (5.5)$$

and

$$\begin{aligned} S_e(f, R) &= \frac{1}{V_{ins}(R)} \sum_a m(a, R) \sigma_e(a, f, R) \\ &= \sum_a n(a, R) \sigma_e(a, f, R) \end{aligned} \quad (5.6)$$

where $n(a, R)$ is the number of bubbles of radius a per volume unit at range R , defined as

$$n(a, R) = \frac{m(a, R)}{V_{ins}(R)} \quad (5.7)$$

For better readability, range dependency is dropped from now in this chapter when writing the equations. Because of the continuous distribution of size, the sums are replaced by the following integrals:

$$M_v(f) = \int_{a=0}^{+\infty} \sigma_{BS}(a, f) n(a) da \quad (5.8)$$

$$S_e(f) = \int_{a=0}^{+\infty} \sigma_e(a, f) n(a) da \quad (5.9)$$

One must notice that shifting from sum to integral changes the unit of n from m^{-3} to m^{-4} . The strict explanation lies in the fact that $n(a)|_{sum} \equiv n(a)da|_{integral}$. *Stricto sensu*, the number of bubbles per unit volum is then $n(a)da$.

5.4 Cross-section and damping constants: first formulas

This section deals with the first formulas that were supposed to be used (especially because they appear both in [2] and [3]). Going through hypothesis, it appears that these equations are limited and can be extended (this is show in section 5.5).

5.4.1 For microbubbles, $ka \ll 1$

It is stated in [2, p. 302] that the cross-sections $\sigma_{BS}(a, f)$ and $\sigma_e(a, f)$ of one single microbubble of radius a , at frequency f and for $ka \ll 1$ (with k the wave number) can be written

as

$$\sigma_{BS}(a, f)|_{ka < 1} = \frac{4\pi a^2}{\left(\frac{f_R^2(a)}{f^2} - 1\right)^2 + \delta^2(a, f)} \quad (5.10)$$

$$\sigma_e(a, f)|_{ka < 1} = \frac{\delta(a, f)}{\delta_r(a, f)} \times \sigma_{BS}(a, f)|_{ka < 1} \quad (5.11)$$

where f_R is the resonance frequency, δ the total damping constant and δ_r the scattering damping constant. The complete theory can be found in [2, chapt. 8] and will not be detailed in this document. It has to be highlighted that these equations are under *clean bubbles in fresh-water assumption*, and that sea-water changes the values of damping constant. The following equations are used for f_R and δ (from [2]):

$$f_R(a, z) = \frac{3.25\sqrt{1 + 0.1z}}{a} \quad (5.12)$$

$$\delta(a, f) = \delta_r(a, f) + \delta_t(a, f) + \delta_v(a, f) \quad (5.13)$$

In these equations, z is the depth from water surface (so is related to range from transducer), δ_t is the damping constant due to thermal conductivity and δ_v is the damping constant due to shear viscosity. These constants are calculated in [2] (calculations are not detailed here), and figure 5.1 shows their evolution for $f = 1$ MHz in absolute value. The other frequencies have the same pattern.

Figure 5.2 shows total acoustical backscattering cross-section $\sigma_{BS}(a)$ of one single bubble of radius a for the four frequencies of the transducer. To each frequency f is associated a resonance radius a_R so that $f_R(a_R, z) = f$. As a matter of information, resonance effect is stronger with lower frequencies.

5.4.2 For bigger bubbles, $ka \gg 1$

It is stated in [2, p. 290] that for larger bubbles ($ka \gg 1$), the backscattering and extinction cross-sections are equivalent to the ones for the "rigid sphere" model. This model is mentioned in [2, p. 270] and the formulas are given in [2, p. 270] and [10]. In this case, the backscattering extinction cross-sections $\sigma_{BS}(a, f)$ and $\sigma_e(a, f)$ are

$$\sigma_{BS}(a, f)|_{ka > 1} = \pi a^2 \quad (5.14)$$

$$\sigma_e(a, f)|_{ka > 1} = 2\pi a^2 \quad (5.15)$$

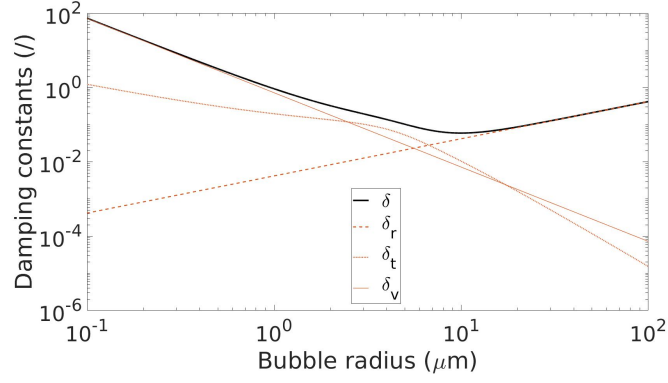


Figure 5.1: Damping constant absolute value over bubble radius @ $z = 1$ m, $f = 1$ MHz
Plotted with [crossSectionCalc.m](#)

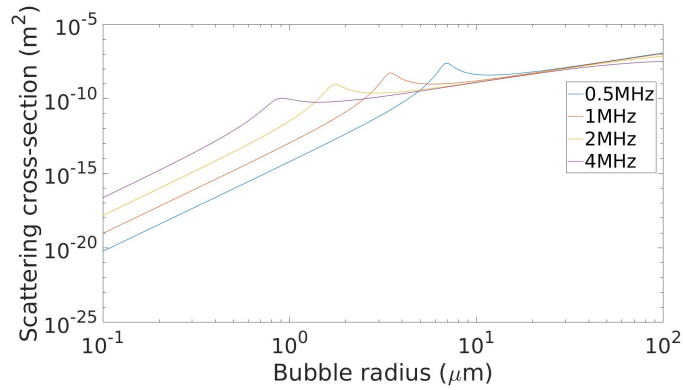


Figure 5.2: Scattering cross-section @ 1 m depth according to particle radius, for $ka \ll 1$
Plotted with [crossSectionCalc.m](#)

5.4.3 Comparison and "all ka " model

Figure 5.3 shows the backscattering cross-section over bubbles radius for the 2 theories: rigid sphere and microbubbles. It can be seen that

1. For $ka \ll 1$, the "microbubbles model" response is way stronger than the "rigid sphere" one,
2. The "microbubbles model" is really not adapted for $ka \gg 1$.

The backscattering cross-section for both $ka \ll 1$ and $ka \gg 1$ is then defined as

$$\sigma_{BS}(a, f) = \begin{cases} \sigma_{BS}(a, f)|_{ka < 1} & \text{when } ka \ll 1 \\ \sigma_{BS}(a, f)|_{ka > 1} & \text{when } ka \gg 1 \end{cases} \quad (5.16)$$

and σ_e follows of course the same equations. σ_{BS} is plotted in figure 5.4 for 4 frequencies (the limit value for ka is here set to 2.16 after reading the intersection x-coordinate).

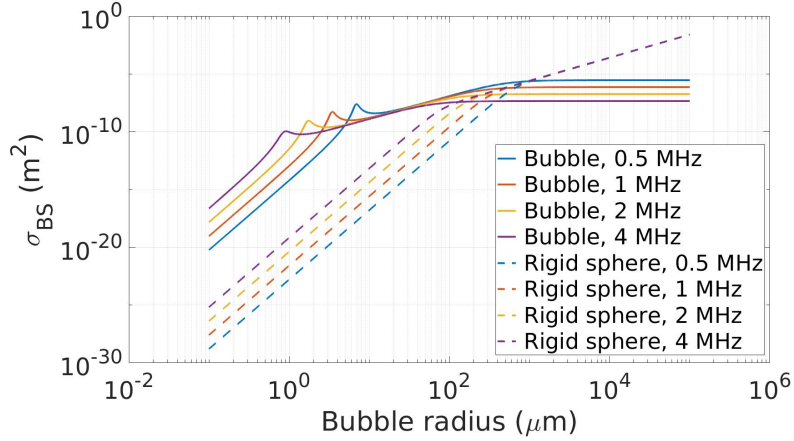


Figure 5.3: Scattering cross-section @ 1 m depth according to different theories
Plotted with [crossSectionCalc.m](#)

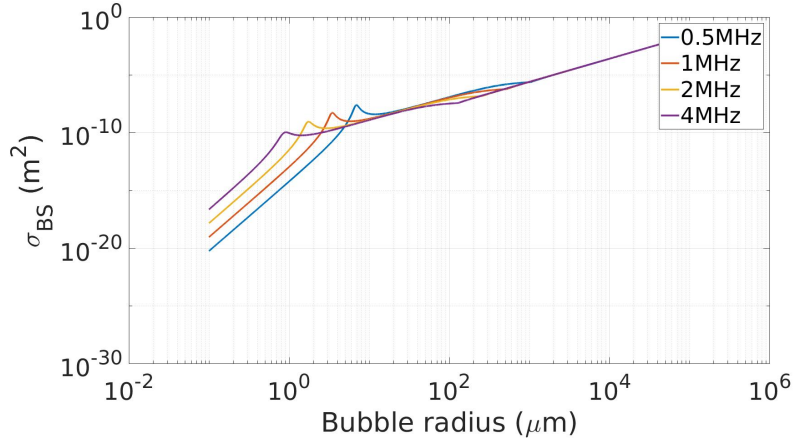


Figure 5.4: Scattering cross-section @ 1 m depth for all ka
Plotted with [crossSectionCalc.m](#)

5.5 Cross-section and damping constants: second and final formulas

In [9] are presented extended formulations close to the ones proposed in section 5.4, but taking into consideration more hypothesis. In particular, an equation for the whole range ka is proposed. Going through the different equations of the document, it appears the parameters (such as damping constants for instance) are the same than used in section 5.4. To lighten the writing, the following notations are used:

$$\begin{aligned}\delta_{tv} &= \delta_t + \delta_v \\ &= \delta - \delta_r\end{aligned}\tag{5.17}$$

The final equations for σ_{BS} and σ_e are

$$\sigma_{BS}(a, f) = \frac{4\pi a^2}{\left(\frac{f_R^2(a)}{f^2} - 1 - \delta_{tv}(a, f)\delta_r(a, f)\right)^2 + \left(\delta_{tv}(a, f) + \frac{f_R^2(a)}{f^2}\delta_r(a, f)\right)^2} \quad (5.18)$$

$$\sigma_e(a, f) = \frac{\delta_{tv}(a, f)}{\delta_r(a, f)} \times \left(1 + \frac{\delta_r(a, f)}{\delta_{tv}(a, f)} + \delta_r^2(a, f)\right) \times \sigma_{BS}(a, f) \quad (5.19)$$

Equations 5.18 and 5.19 are used in the following document, since they cover the whole ka range with only one expression. The damping constants formulations are known, so σ_{BS} and σ_e can be calculated. Figures 5.5 and 5.6 show the backscattering and extinction cross-sections according to the previous equations from [9]. Figures 5.4 and 5.5 can be compared: the curves are the same for small ka , and differ when $ka \gg 1$. Actually, according to [2] and [10], $\sigma_{BS} = \pi a^2$ for large ka , but according to [9], $\sigma_{BS} = 4\pi a^2$. This factor 4 is the difference between the two curves for $ka \gg 1$.

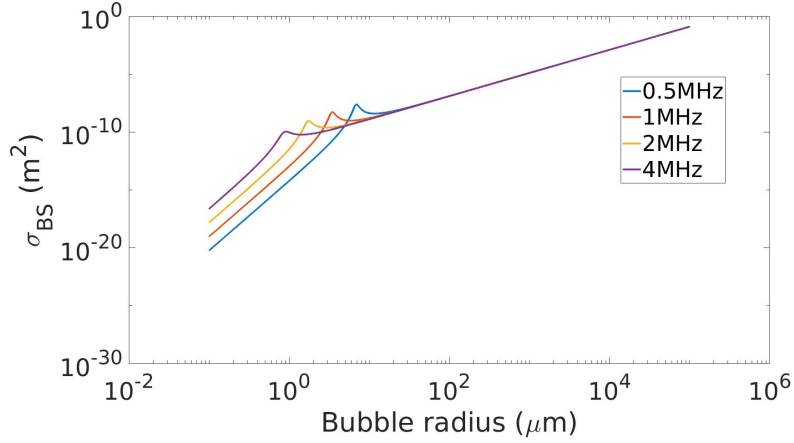


Figure 5.5: Scattering cross-section @ 1 m depth for all ka , from equation 5.18
Plotted with [crossSectionCalc.m](#)

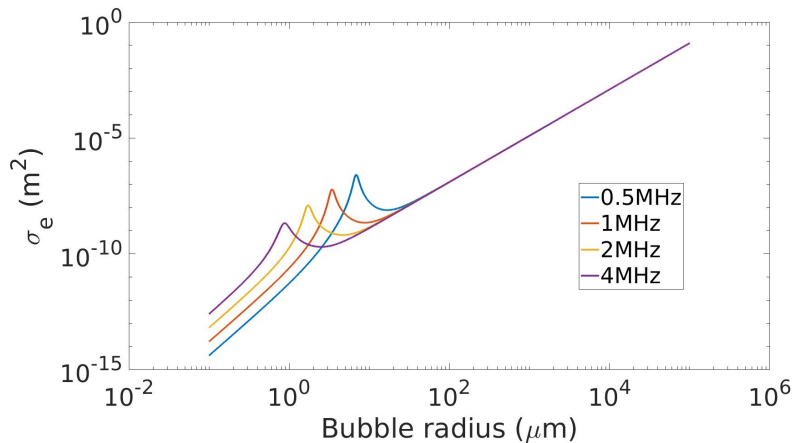


Figure 5.6: Extinction cross-section @ 1 m depth for all ka , from equation 5.19

Figure 5.7 shows the ratio $\frac{\sigma_{BS}}{\sigma_e}$ over the radius range. It can clearly be seen that for a large

enough bubble radius (the limit is around 50 μm), the cross-sections σ_{BS} and σ_e are equal.

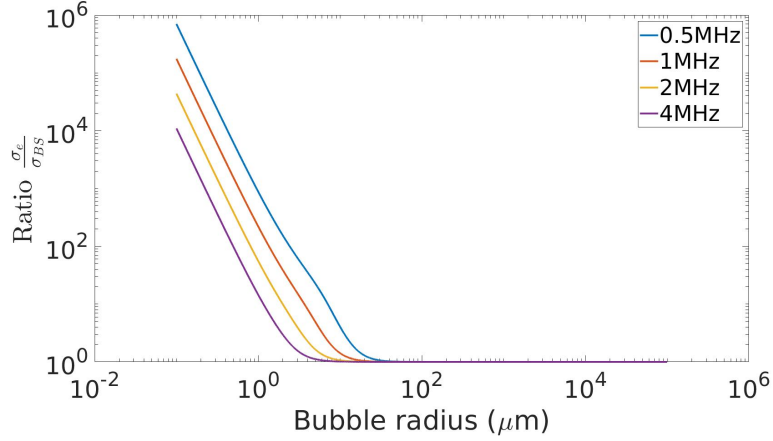


Figure 5.7: Cross-sections ratio @ 1 m depth, from equation 5.19

5.6 Distribution and cross-section per unit volume

Now, to access the distribution $n(a)$ at range R , equations 5.21 should be solved:

$$M_v(f) = \int_{a=0}^{+\infty} \sigma_{BS}(a, f) n(a) da \quad (5.20)$$

$$S_e(f) = \int_{a=0}^{+\infty} \sigma_e(a, f) n(a) da \quad (5.21)$$

These are Fredholm integral equations, where only 4 values are known for $M_v(f)$ at range R .

5.6.1 About the void fraction

The void fraction $q_v(R)$ at range R is defined as

$$q_v(R) = \frac{V_{bubbles}(R)}{V_{ins}(R)} \quad (5.22)$$

where $V_{bubbles}$ is the total volume of bubbles at range R . For only spherical bubbles, it would be defined as

$$V_{bubble} = \frac{4}{3} \pi \int_a m(a) a^3 da \quad (5.23)$$

where, just as a reminder, $m(a)$ is the bubble size distribution in the insonified volume at range R . It can be written, with equation 5.7:

$$\begin{aligned} q_v &= \frac{4}{3}\pi \int_a \frac{m(a)}{V_{ins}} a^3 da \\ &= \frac{4}{3}\pi \int_a a^3 n(a) da \end{aligned} \quad (5.24)$$

In the specific case of only one bubble radius a , the value of void fraction leads to $n(a)$ through

$$n(a) = \frac{3}{4} \frac{q_v}{\pi a^3} \quad (5.25)$$

In general, the "one bubble radius" assumption is wrong, but it can allow to reduce the radius integration range. If q_v is known and the maximum attenuation term $10^{-2 \cdot att}$ can be calculated (this point should be dealt with in chapter 3, but it seems tougher than expected), then a minimum radius can be extracted from tables. Associated with a maximum bubble radius from visual observations, it might allow to frame the radius range.

5.6.2 Issues in solving the equation

The following subsection deals with the issues one reaches when trying to solve equation 5.21.

1. $M_v(f)$ is only known in 4 values. It is not enough to solve the Fredholm equation for the whole radius range (under-determined equations set).
2. Several methods are proposed in [3] to solve the equations sets, based on iterations or matrix computation, but they will be only approached solutions, with a need to interpolate the values for $M_v(f)$.
3. Some assumptions on $\sigma_{BS}(a, f)$ has been tried. Considering the bubble radius is large enough to be in $ka > 1$ area (reminder, k is the wave number), *i.e* where $\sigma_{BS}(a, f) = \sigma_{BS}(a, f)|_{ka>1} = \pi a^2$. This assumption allows to write the following:

$$M_v(f) = \pi \int_{a=\frac{1}{k}}^{+\infty} a^2 n(a) da \quad (5.26)$$

which means $M_v(f)$ is independent from the frequency. This assumption is questionable, and has to be justified case by case. It leads to a loss of information (since the four frequencies are useless), but allows to compute

$$\int_{a=\frac{1}{k}}^{+\infty} a^2 n(a) da$$

which is somehow close to

$$\int_a a^3 n(a) da$$

Combined with assumptions on mean-values, it could lead to something like

$$\int_a a^3 n(a) da \approx \bar{a} \int_a a^2 n(a) da$$

4. There is something to do with q_v and attenuation comparison for high and low frequencies.

Conclusion on high frequency methods

This long part detailed the physical equations under the back-scattering device operation, as well as the progresses that have been done for calibrating the aforesaid device. It also goes through the explanation of what information are needed as a result from the process. The inverse problem solutions have been dropped out before the end, since low-frequencies method (detailed further in part II) seems more promising to meet the project target. However, if this method eventually leads to a deadlock, or if it needs complementary informations to work properly, or again for another use of backscattering in, say, another project, this first part will be a good base to start on.

Part II

Attenuation, sound-speed and low frequency methods

This parts deals with the attenuation and sound-speed variation based method. For a full understanding of what follows, one needs to read over chapter 5 of this report and thesis [1]. Basically, the idea is to used (one-way) attenuation and sound speed measurements to access bubbles population. The setup is described in [11]. Several Matlab scripts have been written to simulate the following process. As stated in part I, this method looks more promising than the ABS one to meet the project target of bubble population measurements. However, even if the theory is now understood enough, experiments has to be conducted in order to confirm or disprove it. To set an example, the water sound speed for a specific set of void fraction, bubble size and wave frequency is supposed to reach values up to 2 or 3 times its usual value, what should be considered cautiously.

Chapter 6

Theoretical background

6.1 Dispersion equation and complex sound speed

Most of the following is based on [5], where is developed a rigorous mathematical model describing the evolution of both phase speed and attenuation of a sound wave in bubbly medium. Leaving apart the complete derivation, the present document starts from the following dispersion equation (6.1. The notations are slightly different in order to match the rest of this report) and takes the same path. The following theory is valid for low void fraction only ([11, p. 2700]), and must be considered cautiously “in the neighborhood of the resonance of the bubbles” ([5, p. 744]).

$$k_m^2 = \frac{\omega^2}{c^2} + 4\pi\omega^2 \int_0^{+\infty} \frac{an(a)}{\omega_R^2 - \omega^2 + j\omega^2\delta(a, \omega)} da \quad (6.1)$$

where k_m is the complex wave number, a the bubble radius, n the bubble distribution, ω is the pulsation and j is the imaginary unit. The inner part of the integral in equation 6.1 looks closely like equation 5.11. The ratio between c and the complex sound speed $c_m = \frac{\omega}{k_m}$ is derived as

$$\frac{c^2}{c_m^2} = 1 + 4\pi c^2 \int_0^{+\infty} \frac{an(a)}{\omega_R^2 - \omega^2 + j\omega^2\delta(a, \omega)} da \quad (6.2)$$

It should be underlined that in [5] is defined a “damping constant” b , that can also be found in [9], and that corresponds to $b = \pi f\delta$. Let be $K = K_1 + jK_2$ the kernel function defined as (see [simuKernel.m](#)).

$$\begin{aligned} K(a, \omega) &= \frac{4\pi c^2 a}{\omega_R^2 - \omega^2 + j\omega^2\delta(a, \omega)} \\ &= \frac{4\pi c^2 a}{(\omega_R^2 - \omega^2)^2 + \omega^4\delta^2} \times (\omega_R^2 - \omega^2 - j\omega^2\delta) \\ &= K_1(a, \omega) + jK_2(a, \omega) \end{aligned} \quad (6.3)$$

so that we can rewrite 6.2 as

$$\frac{c(\omega)^2}{c_m(\omega)^2} = 1 + \int_0^{+\infty} K(a, \omega)n(a)da \quad (6.4)$$

Now let be u and v defined as

$$\frac{c(\omega)}{c_m(\omega)} = u(\omega) - jv(\omega) \quad (6.5)$$

With these notations, u relates to the phase speed of the sound wave, and v relates to the attenuation, and both u and v can be accessed *via* measurements for different frequencies. The method presented below aims to determined the bubbles distribution n . The script [attenuationScript.m](#) deals with this theory and allows to plot the same figures as presented in [5].

6.2 u and v calculation

From an experimental point of view, [11] details how to access u and v from data. Here is an adapted version of these equations. The experimental setup is shown in figure 6.1. The blue ring is the source, while the two red spheres are the receivers (respectively 1 and 2 from right to left). Let be R_1, R_2 the respective ranges of receivers.

There are two ways of calculating u and v . The acoustic theory states that, for an incident source pressure P_s (of pulsation ω and reference range R_0 , see chapter 1), pressures P_1 and P_2 at receivers 1 and 2 are written

$$\begin{aligned} P_s^2 &= P_0^2 e^{j\omega t} \\ P_1^2 &= \frac{P_0^2 R_0^2}{R_1^2} e^{j(\omega t - k_m R_1)} \\ P_2^2 &= \frac{P_0^2 R_0^2}{R_2^2} e^{j(\omega t - k_m R_2)} \end{aligned} \quad (6.6)$$

As we can easily see, the spherical spreading attenuation will play a part in the attenuation calculation. Without bubbles between the source and the first receiver, and since the water attenuation is assumed negligible for these ranges (magnitude 1 m, see section 1.3 for the justification), we can write

$$P_1^2 = \frac{P_0^2 R_0^2}{R_1^2} \exp \left[j\omega \left(t - \frac{R_1}{c} \right) \right] \quad (6.7)$$

Assume that bubbles production between the two receivers can be “turned on and off”. Let subscripts $|_{bubbles}$ and $|_{fresh}$ refer to the situation when bubbles are present and when they are not, respectively. Then we have

$$\begin{aligned} P_2^2|_{fresh} &= \frac{P_0^2 R_0^2}{R_2^2} \exp \left[j\omega \left(t - \frac{R_2}{c} \right) \right] \\ P_2^2|_{bubbles} &= \frac{P_0^2 R_0^2}{R_2^2} \exp \left[j\omega \left(t - \frac{R_1}{c} - \frac{u(R_2 - R_1)}{c} \right) \right] \exp \left[-\frac{\omega R_2 v}{c} \right] \end{aligned} \quad (6.8)$$

There is a little trick here: bubbles are only between the two receivers ! Writing $P_2|_{bubbles}$ the same way P_1 is written with R_2 instead of R_1 **is not correct**.

6.2.1 First way of computation

First way to compute u, v is by using P_1 and $P_2|_{bubbles}$ with bubbles present, so that

$$u = \frac{c}{R_2 - R_1} \times \text{Time delay between the two receivers} \quad (6.9)$$

and by making the ratio of pressures amplitudes (denoted by $\|\cdot\|$), we have

$$v = \frac{c}{\omega(R_2 - R_1)} \times \frac{R_1^2}{R_2^2} \times \ln \frac{\|P_1^2\|}{\|P_2^2\|} \quad (6.10)$$

This method presents the advantage of doing only one experiment to get both u and v . However, the distances R_1, R_2 between the source and the receivers are needed to properly compute the attenuation. It can seem unexpected. It is due to the spherical attenuation, that relates to R^{-2} , so that is not an exponential decrease: the “past” of the signal needs to be known in order to properly compute the attenuation.

6.2.2 Second way of computation

Another way to compute u and v is proposed in [11, p. 2702]. It is based on the difference between pressures P_2 with and without bubbles. Only the attenuation equation changes. The sound speed equation stays the same. From equation 6.8, the attenuation is directly accessed by making the ratio between the pressures amplitudes with and without bubbles:

$$v = \frac{c}{\omega R_2} \times \ln \frac{\|P_1^2|_{fresh}\|}{\|P_2^2|_{bubbles}\|} \quad (6.11)$$

This method does not depend on the distance R_1 anymore, but need two measures, with and without bubbles.

The choice between these two methods is a matter of tradeoff.

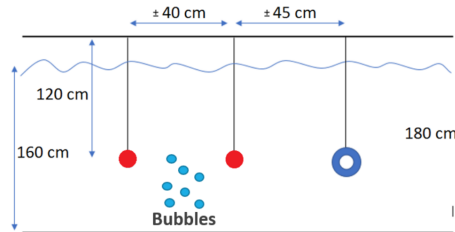


Figure 6.1: Low-frequency experimental setup - figure from [1]

Chapter 7

Kernel inversion process

Based on the theory presented in section 6, a kernel-based inversion process is presented in [11]. This process is detailed here, with some changes in notations. Let be Q , Q_1 and Q_2 defined as

$$\begin{aligned}Q_1(\omega) &= \int_a K_1(a, \omega) n(a) da \\Q_2(\omega) &= \int_a K_2(a, \omega) n(a) da \\Q(\omega) &= Q_1(\omega) + jQ_2(\omega)\end{aligned}\tag{7.1}$$

From equation 6.5 it can be written

$$\begin{aligned}Q(\omega) &= \int_a K(a, \omega) n(a) da = (u - jv)^2 - 1 \\&= u^2 - v^2 - 1 - 2j uv\end{aligned}\tag{7.2}$$

and then

$$\begin{aligned}Q_1(\omega) &= u^2 - v^2 - 1 \\Q_2(\omega) &= -2uv\end{aligned}\tag{7.3}$$

The factor -2 in Q_2 is simplified in [11], so that the equations from the report are slightly different from [11].

7.1 Discretisation

Obviously, from a finite set of pulsations ω_i , one can access only a finite set of u and v , so a finite set of n . [11] proposes to use a linear interpolation on n . The method is detailed below, again slightly different from the article.

It is first assumed that the working radius range can be framed on $[a_{lw}, a_{hg}]$. This interval is then divided in $M - 1$ subdomains, so that M values $n(a_j), j \in \llbracket 1, M \rrbracket$ will be determined.

Linear interpolation is used on this set of values, so that

$$n(a) = \sum_{j=1}^M n(a_j) \varphi_j(a) \quad (7.4)$$

where the M hat functions φ_j are defined as (see [simuPhi.m](#))

$$\varphi_j(a) = \begin{cases} 0 & \text{if } a < a_{j-1} \\ \frac{a - a_{j-1}}{a_j - a_{j-1}} & \text{if } a_{j-1} \leq a < a_j \\ \frac{a_{j+1} - a}{a_{j+1} - a_j} & \text{if } a_j \leq a < a_{j+1} \\ 0 & \text{if } a_{j+1} \leq a \end{cases} \quad (7.5)$$

Equations 7.1 and 7.4 lead to

$$\begin{aligned} Q(\omega) &= \int_{a_{lw}}^{a_{hg}} K(a, \omega) \sum_{j=1}^M n(a_j) \varphi_j(a) da \\ &= \sum_{j=1}^M n(a_j) \int_{a_{lw}}^{a_{hg}} K(a, \omega) \varphi_j(a) da \end{aligned} \quad (7.6)$$

7.2 Matrix-form writing

For a given number of pulsations nbF , we have $\omega_i, i \in \llbracket 1, nbF \rrbracket$ and equation 7.6 can be written in matrix form:

$$\mathbf{Q} = \mathbf{\Gamma} \times \mathbf{n} \quad (7.7)$$

where

$$\begin{aligned} \mathbf{Q} &= \left[Q(\omega_i) \right]_{i,1} \\ \mathbf{\Gamma} &= \left[\int_{a_{lw}}^{a_{hg}} K(a, \omega_i) \varphi_j(a) da \right]_{i,j} \\ \mathbf{n} &= \left[n(a_j) \right]_{j,1} \end{aligned} \quad (7.8)$$

One must not overlook that equation 7.7 is actually a set of 2 equations, dealing respectively with Q_1, K_1 and Q_2, K_2 . [11] states that using the second kernel leads to better results than using the first one. However, this discrimination is not used in the simulation.

7.3 Problem inversion

Equation 7.7 should now be inverted. As stated previously, two inversions can take place, relating to the two kernels. In [11] is proposed constrained inversion, especially with Tikhonov method. Different methods are tested in `simulationScript.m`. This script works as follow:

1. Simulation of a distribution $n(a)$ over radius range $[a_{lw}, a_{hg}]$ (mainly sum of normal distribution, but this can be changed in `simuDistrib.m`). The script also allows to control the adequation between the radius range and the set of frequencies.
2. Simulated u and v from the distribution and the chosen set of frequencies, pure or with noise/offset (see `simuDisp.m`).
3. Calculations of Q_1 and Q_2 from u and v .
4. Calculation of hat functions φ_j (see `simuPhi.m`), kernels K_1 and K_2 (see `simuKernel.m`) and integrated discretized kernel (see `simuKPhi.m`).
5. Different inversion processes (see below), in order to output two solutions for \mathbf{n} , relatively to K_1 and K_2 .
6. Along the script, most of the simulated and calculated values can be plotted, and step-controls are written on the way.

The different methods used to invert the problem are enumerated below. The explanations only give a rough idea of how behave the method, and strongly depends on the noise level, the simulation etc. These methods give \mathbf{n} from both kernels, as well as their mean value, so that 3 solutions are available. Smoothing function (5-points moving average) can be applied to reduce oscillations: usually, it deteriorates the solutions for non-noisy data, but increases the quality for oscillating solutions.

PSINVM Pseudo-inverse method, based on built-in Matlab function `pinv`. No constraint, the calculation is simply $\mathbf{n} = \mathbf{\Gamma}^\dagger \times \mathbf{Q}$, where \dagger denotes the Moore-Penrose pseudo-inverse, and the negative values are replaced by zero. It seems that this method gives usable results when $2 \times nbF < M < 3 \times nbF$. Below, the inversion is totally inaccurate. Above, the solution starts to overfit. The accuracy of the solution strongly depends on the simulated distribution.

NNLSM Non-negative least-square method. The only constraint is the non-negativity of the solution. Based on the built-in Matlab function `lsqnonneg`. It gives rather good result for pure u and v up to $M = 1.5 \times nbF$, then starts to overfit and oscillate. For noisy data, the inversion deteriorates fast for $M > 0.5 \times nbF$. For these values of M , it seems that the method is robust to offset.

LSQLIN Based on built-in function `lsqlin`, this method allows to constrain the solution as proposed in [11, p. 2705]. More generally, and according to Matlab documentation, this function solves least-squares curve fitting problems of the form

$$\min_x \frac{1}{2} \|C \cdot x - d\|_2^2 \quad \text{such that} \quad \{A \cdot x \leq b \quad \text{and} \quad A' \cdot x = b' \quad \text{and} \quad lb \leq x \leq ub\}$$

Even though the function itself accepts a reduced number of input argument, it seems in our case that a usable value can be obtained only with correct bounds $lb \leq x \leq ub$. For instance, using simply $0 \leq x \leq \infty$ gives inaccurate results, with or without noise.

TRM Tikhonov regularization based method. Function `tikhonov` comes from [12], and its operation is described in the associated documentation. The different constraints are included in a regularization parameter λ that must be supplied to the function. That being said, determining this parameter is rather tough: the proposed method is then experimental testing by means of the simulation script. It must be underlined that a function version of `simulationScript.m` is written under `simuInversion.m`, intended to be used together with `simulationIter.m` in order to experimentally tune the regularization parameter. In our case, for a parameter around 10^{-13} and without noise, the solutions perfectly fit the simulated distribution on a range $0.3 \times nbF < M < 10 \times nbF$ (bigger values have not been tested). The solutions are less accurate for noisy data (oscillations), but smoothing allows to get really acceptable results for $1.25 \times nbF < M < 2.5 \times nbF$. The methods seems quite robust to offset without noise, but shows troubles dealing with noise and offset simultaneously.

One must notice:

- M and nbF parities play a part in the accuracy of proposed solution for every method. I think (and this is only feelings) that, from a numerical point of view, some couples (M, nbF) will work better than others, maybe due to prime number or divisibility issues.
- To get an accurate behaviors of the method, many different distributions should be tested. Even though the Matlab implementation of such a thing is easy, the calculation time increases rapidly.
- The simulation clearly shows that reducing the noise with multiple measurements leads to better inversions.

Other observations are made in the next chapter, illustrated for a specific set of frequencies.

Chapter 8

Case study: [20-90] kHz measurement band

In this chapter is specifically studied the inversion process for available data from [20-90] kHz measurements. It is based on the frequencies of the transducers used in [1]. It allows to point out both general and specific observations about the inversion process.

8.1 Shape of Q_1 and Q_2

Experimentally, the inversion turns out well if Q_1 and Q_2 over frequency present specific shapes, shown in figure 8.1, and that these shapes are described by enough points.

Both the shape and the amplitude of Q_1, Q_2 are of importance in inversion. Figure 8.2 shows the evolution of amplitude for different void fraction (the bubble size distribution is a normal distribution centered on 90 μm with 10 μm of standard deviation and an amplitude between 10^{10} and 10^{13} m^{-4}). The shapes stay the same but the amplitudes increase with the void fraction.

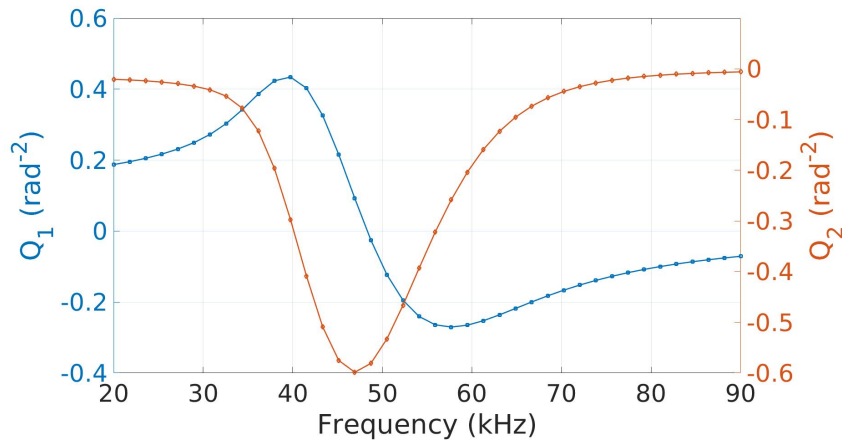


Figure 8.1: Specific shapes of Q_1 and Q_2 (mind the y-axes)

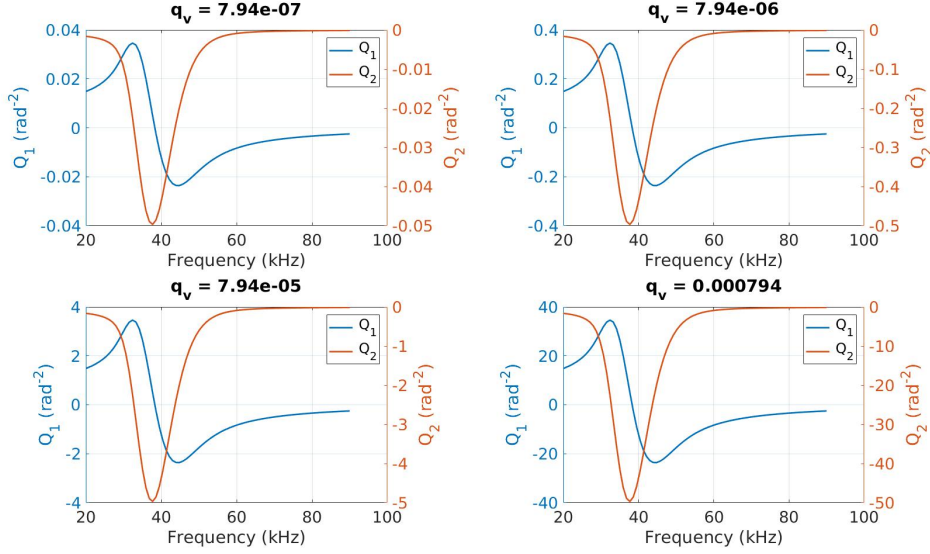


Figure 8.2: Specific shapes of Q_1 and Q_2 (mind the y-axes) for different values of q_v

8.2 Frequency and radius

The harmony between the frequency band and the working radius range is important, since one will not be able to inverse the problem for any radius range from a specific frequency band. This harmony seems to strongly depends on the resonance frequency defined in equation 5.13. Figures 8.3 and 8.4 show the kernels K_1 and K_2 for frequencies between 20 kHz and 90 kHz, along a large radius range. Three parts (roughly) can be distinguished:

1. Below 30 μm . For all the considered frequencies, K_1 and K_2 are flat and almost zero. If the distribution is concentrated in this area, the shape for Q presented in section 8.1 is shown figure 8.7. The characteristic shape is not fully described, which lead to poor inversion.
2. Between 30 μm and 0.3 mm. K_1 and K_2 are varying there, around their resonance radius a_R , and at least one frequency always differs from the others. Figures 8.5 and 8.6 show the kernel plotted on this specific part. The legends are removed for readability, and more frequencies are plotted. Working in this range makes the shape of Q_1 and Q_2 quite centered in the frequency band and fully described: it looks like the best option for an accurate inversion.
3. Above 0.3 mm. Smooth variations, the patterns are the same. If the distribution n is concentrated there, the shapes of Q_1 and Q_2 are crushed on the left of the frequency band: badly described, it leads to poor inversion.

Back to section 8.1 and equation 7.1, it can be seen that Q is defined by integrating the product $K \times n$ over radius. Now, for increasing radius and decreasing frequency, the amplitudes of the peaks increase for both K_1 and K_2 . For a given frequency, a small amount of large bubbles has then the same or even a stronger effect than a large amount of little bubbles.

One must notice that no experiment has been carried out by SiPLAB to confirm or disprove the previous theory. More, as stated in section 6, this theory must be considered cautiously

around the resonance radius of the bubbles, and this resonance neighborhood is *de facto* of a major significance in the inversion. This theory limit can easily be seen when plotting u for large bubbles: for instance, a modal distribution centered on $160\ \mu\text{m}$ for a void fraction $q_v = 8.7 \cdot 10^{-5}$ theoretically leads to $u(30.8\ \text{kHz}) = 8.78$, which seems absolutely impossible.

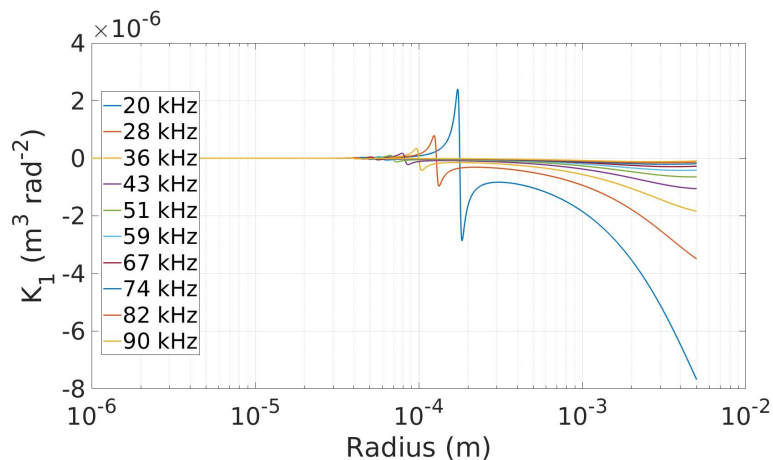


Figure 8.3: Kernel K_1 for a large radius range

8.3 Inversion processes

It is right now difficult to extract precise results about inverse solutions quality, especially because it depends on the simulated distribution, the void fraction q_v , the parameter M , the number of frequencies nbF or the different inversion parameters (λ for Tikhonov regularization, bounds for constraints least-squares...). However, from a certain number of iterations, it seems that Tikhonov regularization method (TRM) gives the best results. For this reason, tuning the parameter λ is of importance. As stated in section 7.3, the theoretical way (developed in [13]) to choose this parameter is difficult to understand (= I did not succeed), so an iterative method is used to do so.

Figure 8.9 shows 3 sets of simulated distribution used to tune λ . They are chosen so that

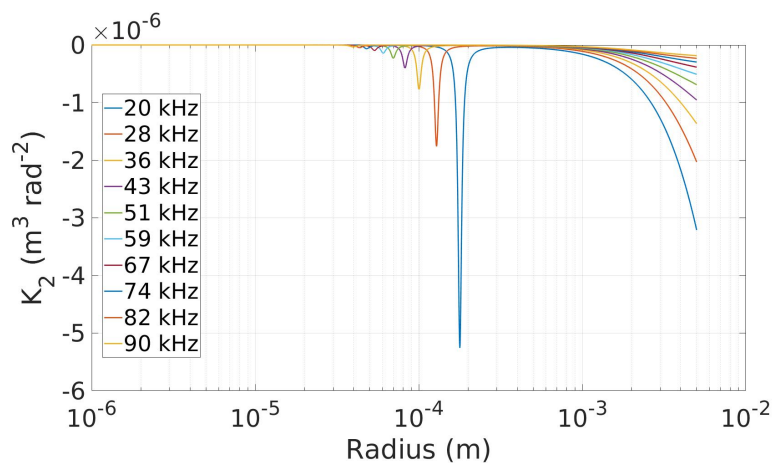


Figure 8.4: Kernel K_2 for a large radius range

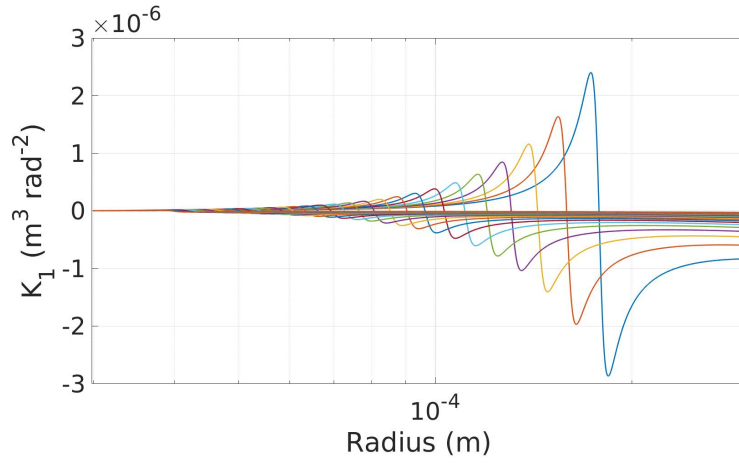


Figure 8.5: Kernel K_1 for a radius range centered on the resonating radius, for $f = [20 - 90]$ kHz

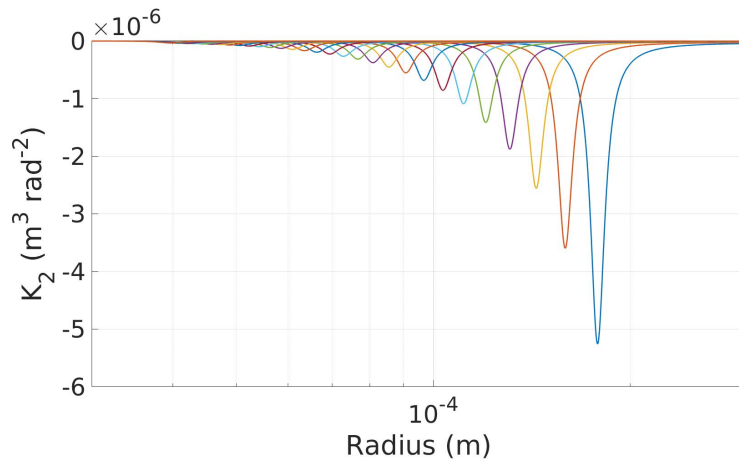


Figure 8.6: Kernel K_2 for a radius range centered on the resonating radius, for $f = [20 - 90]$ kHz

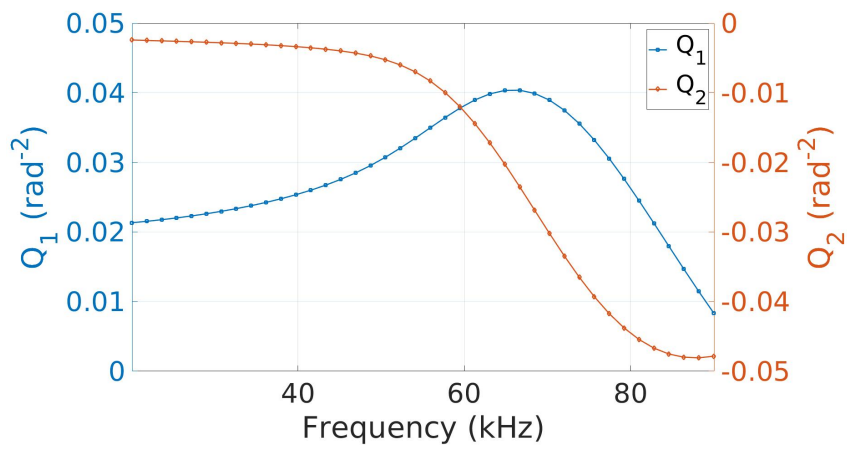


Figure 8.7: Q_1 and Q_2 shapes for a normal distribution centered on $30 \mu\text{m}$

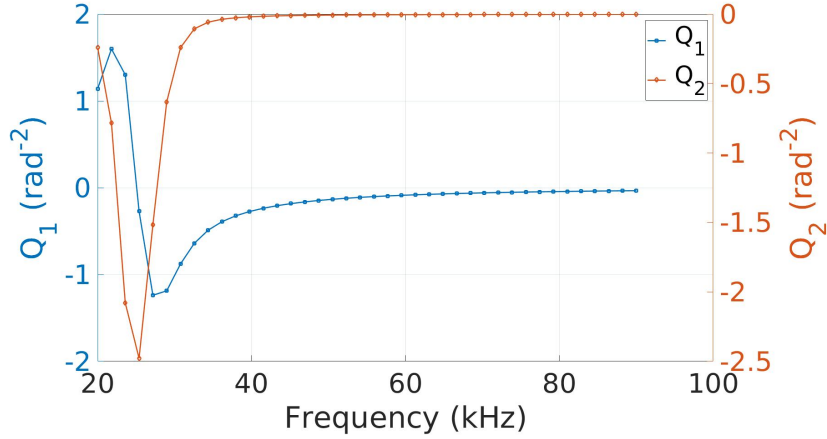


Figure 8.8: Q_1 and Q_2 shapes for a normal distribution centered on 140 μm

$q_v \approx 2.5 \cdot 10^{-6}$. They are normal distributions of standard deviation 10 μm , centered respectively on 60, 90 and 120 μm , with amplitudes of $100 \cdot 10^9$, $35 \cdot 10^9$ and $13 \cdot 10^9 \text{ m}^{-4}$. These sets are then inversed with TRM for different values of M and λ . As stated earlier, two solutions are available every time, based on the two kernels K_1 and K_2 (the mean results is not used in this case).

To summarize the results quality, Pearson correlation coefficients ρ are used. These coefficients have a strong limitation, since they only characterize the correlation between the solutions and the simulated distribution. The amplitude of the solution does not appear in the coefficient. In our specific case of Tikhonov inversion, no amplitude difference could be seen, but for another process, the calculation of the amplitudes ratio inversed solution/simulated distribution is of importance.

Figures 8.10, 8.11 and 8.12 show the evolution of correlation coefficient ρ for the three distributions, the two kernels processes, without noise and offset, for 40 frequencies and λ between 10^{-15} and 10^{-10} . It can be seen that whichever M is used between $0.5 \times nbF$ and $2 \times nbF$, λ between 10^{-15} and 10^{-13} leads to good inversion. Of course, a smaller step for λ can be chosen for a finer tuning.

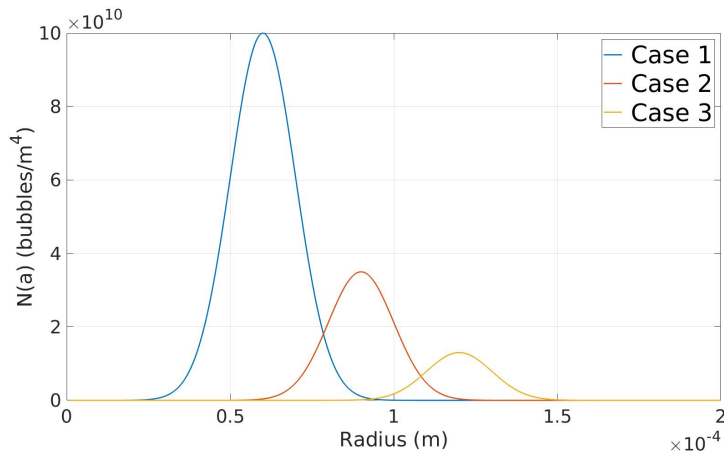


Figure 8.9: Set of distributions for inversion
The 3 distributions lead to $q_v \approx 2.5 \cdot 10^{-6}$

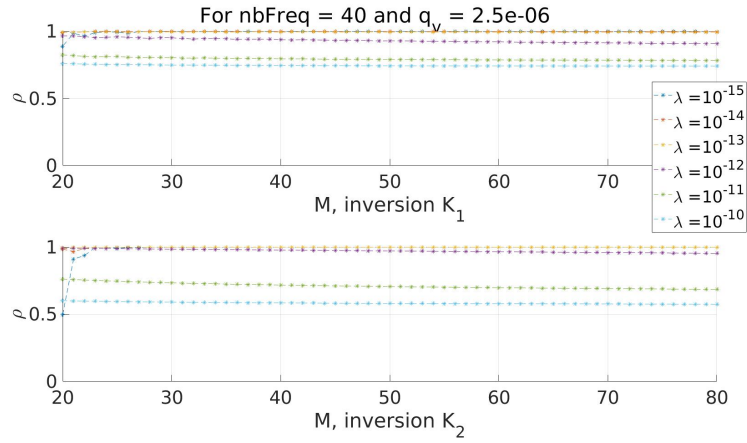


Figure 8.10: Correlation coefficients ρ over M for distribution of case 1

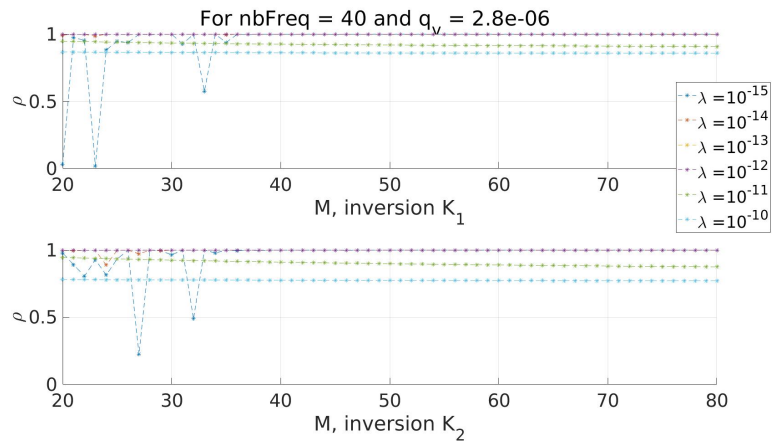


Figure 8.11: Correlation coefficients ρ over M for distribution of case 2

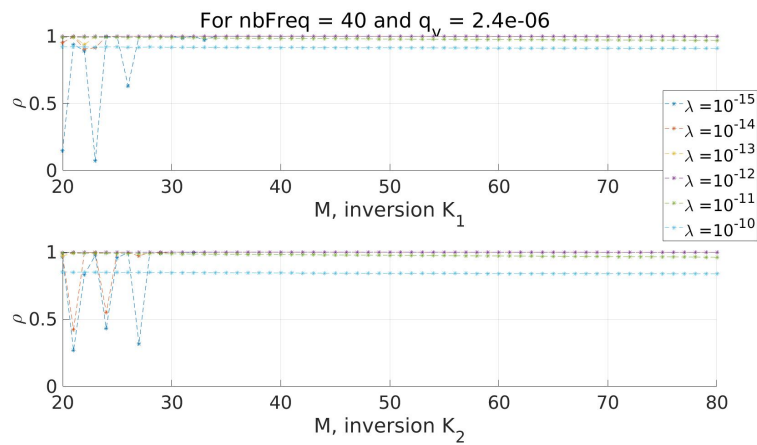


Figure 8.12: Correlation coefficients ρ over M for distribution of case 3

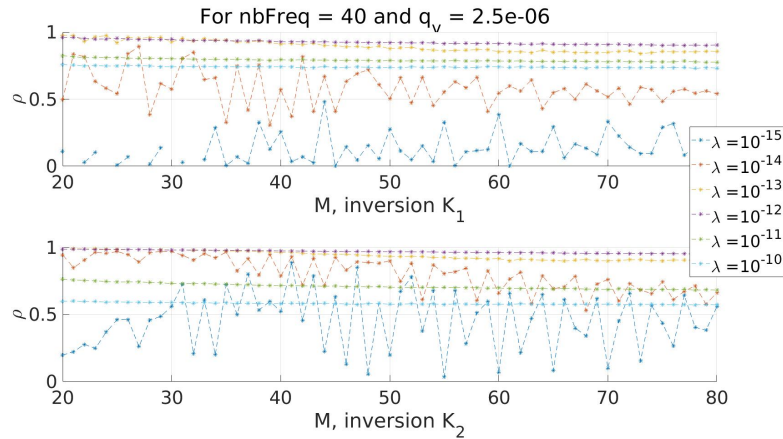


Figure 8.13: Correlation coefficients ρ over M for distribution of case 1, with noise

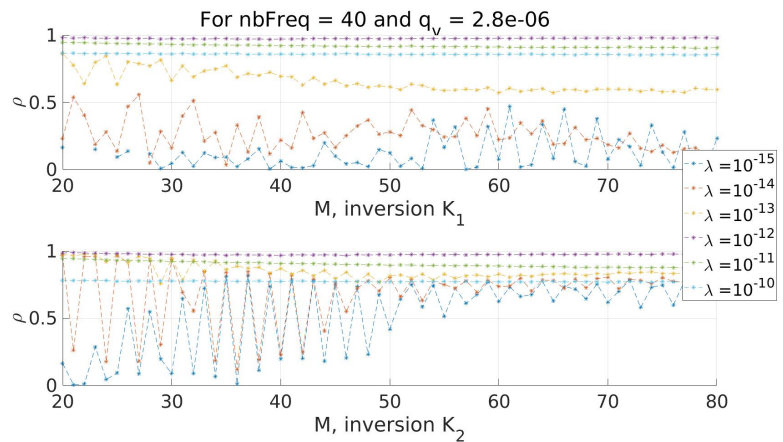


Figure 8.14: Correlation coefficients ρ over M for distribution of case 2, with noise

Figures 8.13, 8.14 and 8.15 show the evolution of correlation coefficient ρ for the three distributions, the two kernels processes, without offset but with noise, for 40 frequencies and λ between 10^{-15} and 10^{-10} . Since the noise is added “randomly” in the simulation script (normal noise up to 1% on u and up to 20% on v), 100 iterations are operated, and the ρ values are averaged. The results are given for what they are worth, since 100 iterations are not proved to be better than twice or ten times more. Furthermore, the time needed to run these simulations is roughly 80 minutes each, which is long enough. Further simulations can be runned if necessary. Assuming the following results make sense, it allows anyway to observe some points:

- The couple (nbF, M) has a strong influence on the solution accuracy. In particular, the parity of M for kernel 2 inversion, case 2, for $\lambda = 10^{-14}$ or 10^{-15} plays as strong part in the correlation coefficient.
- The best results are obtained for λ around 10^{-12} . The simulation could be done again with a smaller step on λ to get a more precise value. One can also notices that choosing λ in this situation would be a trade off between the three cases 1, 2 and 3.
- A limit for M appears in cases 2 and 3 for K_2 inversion method.

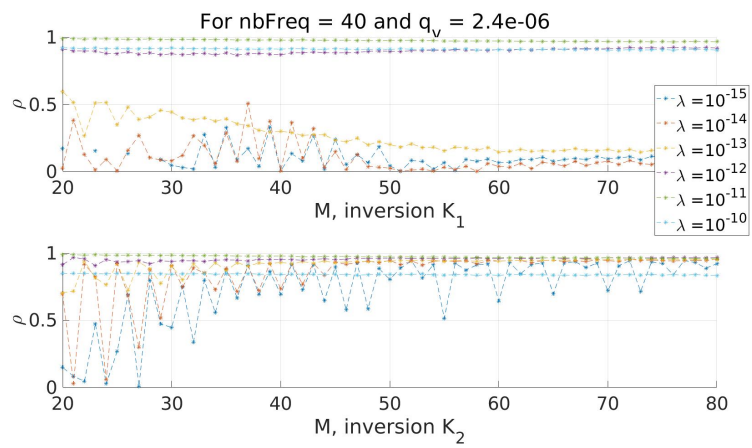


Figure 8.15: Correlation coefficients ρ over M for distribution of case 3, with noise

Conclusion on low frequency methods

In this part has been developed the theory related to attenuation and sound speed modification of acoustic wave by bubbly medium, and its use as a tool to access the bubble population according to bubble size and void fraction.

Even though this inversion theory is well explained in paper and correctly implemented by simulation, experiments must be carried out in order to confirm or disprove the feasibility and accuracy of such a method. In particular, the high values of sound speed predicted by the theory seems rather unrealistic. The experimental setup, as well as the raw data (u and v) processing needs to be taken care of. One should go through [1] and [11] for this purpose.

Another limitations of this method lies on the available frequencies: the bubbles radius range is not known yet, and the current devices available for the experiment are limited between 20 and 90 kHz, which lead to a radius range between 30 μm to 0.3 mm *maximum*, while an experiment conducted by our biologists teammates show bubbles that were visible to the naked eye. For the moment, nothing proves that such big bubbles can lead to usable inversion with this set of frequencies.

No inverse solutions are plotted in this document, since they highly depend on the distribution, the couple nbF, M , the set of frequencies, the noise, the offset and the methods used to inverse the problem, and so the usefulness of such plots would be only aesthetic. It is strongly recommended to play with [simulationScript.m](#) as the same time as reading the current report in order to fully understand all the above.

Part III

Appendix, notations, Matlab files and bibliography

Appendix

Mathematical justification of the integration

This section aims to justify the following equivalence:

$$\int_{\rho=R-\frac{L}{2}}^{R+\frac{L}{2}} \frac{1}{\rho^4} \rho^2 d\rho \underset{R \gg \frac{L}{2}}{\sim} \frac{1}{R^4} \int_{\rho=R-\frac{L}{2}}^{R+\frac{L}{2}} \rho^2 d\rho \quad (8.1)$$

Let be, for better visibility, $\frac{L}{2} = h$. For the left part of equation 8.1 we have:

$$\begin{aligned} \int_{\rho=R-h}^{R+h} \frac{1}{\rho^2} d\rho &= \frac{1}{R-h} - \frac{1}{R+h} \\ &= \frac{2h}{R^2 - h^2} \\ &= \frac{1}{R^2} \frac{2h}{1 - \left(\frac{h}{R}\right)^2} \\ &\underset{R \gg h}{\sim} \frac{2h}{R^2} \end{aligned} \quad (8.2)$$

And for the right part of equation 8.1 we have:

$$\begin{aligned} \frac{1}{R^4} \int_{\rho=R-h}^{R+h} \rho^2 d\rho &= \frac{1}{3R^4} ((R+h)^3 - (R-h)^3) \\ &= \frac{1}{3R^4} (2h^3 + 6R^2h) \\ &= \frac{2h}{R^2} \left(\frac{1}{3} \left(\frac{h}{R}\right)^2 + 1 \right) \\ &\underset{R \gg h}{\sim} \frac{2h}{R^2} \end{aligned} \quad (8.3)$$

Equations 8.2 and 8.3 justify the integration method in section 1.1. This equivalence has also been verified with Matlab.

Equations proposed by AQUAtec and near-range correction

The AQUAtec device follows equations for calibration and inversion method provided by [14], in particular equation 8.4:

$$V_{rms} = \frac{K_s K_t \sqrt{M}}{R\xi} e^{-R\alpha'} \quad (8.4)$$

where V_{rms} is the backscattered signal, K_s contains the sediment backscattering properties, M is the sediment concentration, ξ is the near-field correction and K_t is the system constant, taking into account the characteristics of the device. The near field correction factor ξ is calculated as shown in equations 8.7 and 8.8, according to [8] or AQUAtec respectively. In both equations are used the parameters R_n and Z , defined in equations 8.5 and 8.6. The ξ factor is plotted in figure 8.16 with both approaches from [8] and AQUAtec as a function of Z .

$$R_n = \frac{\pi A_t^2}{\lambda} \quad (8.5)$$

$$Z = \frac{R}{R_n} \quad (8.6)$$

$$\text{According to [8]: } \xi = \frac{1 + 1.35Z + (2.5Z)^{3.2}}{1.35Z + (2.5Z)^{3.2}} \quad (8.7)$$

$$\text{According to AQUAtec: } \xi = \begin{cases} 1 & \text{if } Z > 2 \\ \frac{1}{3}(2 + \frac{2}{Z}) & \text{if } Z < 2 \end{cases} \quad (8.8)$$

Equation 8.4 is actually equivalent to equation 1.30 (both are from the propagation equation). The squared version of equation 8.4 is

$$V_{rms}^2 = \frac{K_s^2 K_t^2 M}{(R\xi)^2} e^{-2R\alpha'} \quad (8.9)$$

with V_{rms}^2 equivalent to v_r^2 , M equivalent to M_v , $\frac{1}{(R\xi)^2}$ the spherical propagation and $e^{-2R\alpha'}$ the range dependent attenuation equivalent to $10^{-\frac{2\alpha(R-R_0)}{10}}$ (please note α and α' coefficients are different).

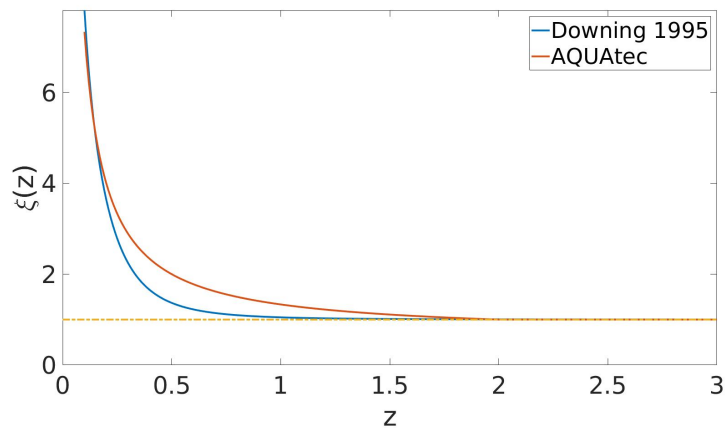


Figure 8.16: Near range factor ξ from AQUAtec and from [8]

Notations

Symbol	Unit	Description
α	dB m ⁻¹	Total attenuation coefficient
α_w	dB m ⁻¹	Attenuation coefficient from water
α_b	dB m ⁻¹	Attenuation coefficient from bubbly medium ([2])
$\Delta\sigma_{BS}$	m ²	Differential cross-section
δ	/	Total damping constant
δ_r	/	Scattering damping constant
δ_t	/	Thermal damping constant
δ_v	/	Viscous damping constant
δ_{tv}	/	(<i>Notations</i>) $\delta_t + \delta_v$
$\mathbf{\Gamma}$	m ⁴ rad ⁻²	Matrix of integrated discretized kernel
ω	rad s ⁻¹	Pulsation
λ	/	Tikhonov regularization parameter
ω_R	rad s ⁻¹	Resonance pulsation
ϕ	rad	Azimuth (polar coordinates)
ρ	/	Pearson correlation coefficient
φ	/	Hat function
ψ_{BP}	sr	Ideal beam pattern
ψ	sr	Integrated beam pattern according to [2]
σ_{BS}	m ²	Backscattering cross-section
σ_e	m ²	Extinction cross-section
τ	s	Profile length
Θ	°C	Water temperature
θ	rad	Elevation (polar coordinates)
θ_{mx}	rad	Opening angle, define the insonified volume
ξ	/	Near field correction
a	m	Bubble radius
a_R	m	Bubble resonance radius
a_{lw}, a_{hg}	m	Bubbles radius limits (to frame the range)
att	dB	Total attenuation from water and bubbly medium
A_t	m	Transducer radius
B_t	m ⁻²	Attenuation from bubbly medium

Symbol	Unit	Description
c	m s^{-1}	Free bubble water sound speed
c_m	m s^{-1}	Complex sound speed
C_0^2	$\text{V}^2 \text{m}^3$	Device constant defined as $C_0^2 = v_s^2 H_{sr}^2 \frac{R_0^2}{4\pi} \psi L$
D_t	/	Source directivity
D_r	/	Receiver directivity
d^3V	m^3	Spherical elementary volume
$E(x)$	$[\text{x}]^2$	Energy of signal x
f	Hz	Frequency
f_R	Hz	Resonance frequency
f_{prof}	Hz	Profile rate (device)
G_s	Pa V^{-1}	Voltage to pressure gain of the source
H_{sr}	/	Product of gains G_s and K_r
h_w	m	Water height (from tank bottom)
I_s	W	Incident sound wave intensity
J_1	/	First order first kind Bessel function
k	m^{-1}	Wave number
k_m	m^{-1}	Complex wave number
K_r	V Pa^{-1}	Pressure to voltage gain of the receiver
K	$\text{m}^3 \text{rad}^{-2}$	Kernel function
K_1	$\text{m}^3 \text{rad}^{-2}$	Kernel function, real part
K_2	$\text{m}^3 \text{rad}^{-2}$	Kernel function, imaginary part
L	mm	Bin size or resolution
$ L_s $	m	Backscattering length
M_v	m^{-1}	Backscattering cross-section per unit volume
M	/	Number of points for the interpolation of N
m_{prof}	/	Number of stored profiles (device)
$m(a)$	/	Number of bubbles of radius a
$n(a)$	m^{-3} or m^{-4}	Number of bubbles of radius a per unit volume
nbF	/	Number of frequencies
\mathbf{n}	m^{-3} or m^{-4}	Matrix of bubble population for specific radius a_j
N	/	Number of bins (device)
N_0	/	Start bin (device)
N_L	/	Number of bins (device)
P_0	Pa	Reference pressure from the source at R_0
P_1, P_2	Pa	Pressure recorded at receivers 1 and 2 (section 6)
P_s	Pa	Incident pressure from the source
P_{scat}	Pa	Scattered pressure
P_r	Pa	Pressure received by the transducer
dP_r	Pa	Elementary pressure received by the transducer
q_v	/	Void fraction

Symbol	Unit	Description
Q	rad^{-2}	Integrated population-weighted kernel
Q_1	rad^{-2}	Real integrated population-weighted kernel
Q_2	rad^{-2}	Imaginary integrated population-weighted kernel
\mathbf{Q}	rad^{-2}	Matrix of Q_1 or Q_2
R	m	Range
r	m	Range (polar coordinates)
R_0	m	Reference range for the pressure
R_1, R_2	m	ranges of receivers 1 and 2 (section 6)
R_{ref}	m	Reference range for the calibration
R_{max}	m	Maximum range (from transducers)
R_{min}	m	Minimum range (from transducers)
ΔR_{eff}	m	Effective measured range
R_x^{dB}	dB	Gain relative to default(device)
RL	dB	Receiver level (sonar equation)
SL	dB	Source level (sonar equation)
S_e	m^{-1}	Extinction cross-section per unit volum
SNR	/	Signal to noise ratio
T_{burst}	s	Burst length (device)
T_{int}	s	Burst interval (device)
T_x^{dB}	dB	Transmit power (device)
TL	dB	Transmission losses (sonar equation)
TS	dB	Target strength (sonar equation)
V_G	m^3	Volume defined as $\frac{1}{3} \left((R + \frac{L}{2})^3 - (R - \frac{L}{2})^3 \right)$
V_{ins}	m^3	Insonified volume (usually defined at range R)
$V_{bubbles}$	m^3	Total volume of bubbles
v_s	V	Input voltage transducer
v_r	V	Output voltage transducer
z	m	Depth from water surface
$(x)^{dB}$	dB	Refers to decibel version of object (x)
$(x)_{ref}$	[x]	Refers to reference experiment for calibration
$\ (x)\ $	[x]	Refers to amplitude of object (x)
$(x) _{bubbles}, (x) _{fresh}$	[x]	Refer to presence or absence of bubbles
$(\mathbf{X})^\dagger$	/	Refers to Moore-Penrose pseudo-inverse of matrix \mathbf{X}

Matlab files

Scripts

Name	Description	In the report
ABSinversion.m	This script processes the ABS raw data from long-time experiment (for this report, 2016, July 26 experiment) and try to invert the problem.	Section 5.2
attenuationScript.m	Calculations and plots of attenuation and sound speed according to [5]	Equation 6.5
calibration150218.m	This script processes the ABS data from the first calibration experiment (2018,February 15)	Chapter 4
crossSectionCalc.m	Calculations and plots of cross-sections σ_{BS} and σ_e according to [2], [9] and [10]	Figures of chapter 5
cyclesNumber.m	Automate the calculation of maximum number of cycles for the low-frequency setup presented in [1]. Not used in this report, but allows to save time when preparing the experiment.	/
directivity.m	Computes and plots the device directivity and the values of θ_{mx}	Chapter 2 and table 1.1
exportConvertABS.m	To convert ABS data from *.aqa to *.mat. Used if AQUAtec toolkit does not work. Based on function ReadAquaScat1000.m	Chapter 3
misc_calculations.m	Miscellaneous calculations: near range modification factor, resonance radius and water attenuation coefficient.	Figurea 1.4, 3.6 and 8.16
plotData_2D.m	To plot ABS data from 'one-shot' experiment, i.e with no time-continuity (e.g calibration). It has not been used for this work.	/

Name	Description	In the report
plotData.3D.m	To plot ABS data from 'time-continuous' experiment. It has been essentially used to plot data from experiment of 2016, July 26.	Figures 3.1 to 3.4
simulationIter.m	This script calls function simuInversion.m in loops, in order to tune Tikhonov parameter λ	Figures 8.13 to 8.15
simulationScript.m	Simulation of the low-frequency theory presented in [11]. It creates a bubbles distribution, simulates the experimental data and use different processes to invert the problem.	Chapters 7 and 8

Functions

The informations in column *Associated script(s)* are non-exhaustive.

Name	Description	Associated script(s)
attenuationFctCP.m attenuationFctMC.m	Compute attenuation terms due to bubbly medium from different theories.	attenuationScript.m
crossSectionAinslie.m crossSectionMedwin.m crossSectionStanton.m	These functions compute cross-sections according to different theories	crossSectionCalc.m
DampingCste.m	Computes damping constants $\delta, \delta_r, \delta_v, \delta_t$ according to [2]	crossSectionCalc.m
Directiv.m	Computes ABS directivity D_t according to [2]	directivity.m
InitialAttenuation.m	(ABS data) Computes attenuation term @ surface range, taking the whole working range into account.	ABSinversion.m
InsonifiedVolume.m	Computes ABS insonified volume V_{ins} according to equation 1.25	ABSinversion.m
IntBeamPatt.m	Computes ABS integrated beam pattern ψ according to equation 2.2	ABSinversion.m
loadABS_Data.m	Loads and adapts ABS data for a long time experiment. Unadapted for calibration experiment	Many
loadAquatecData.m	Loads the usual characteristics of AQUAtec backscattering device (ABS)	Many

Name	Description	Associated script(s)
RangeFiltering.m	(ABS data) Applies a median filter on the proposed signal along range (see function TimeFiltering.m)	ABSinversion.m
ReadAquaScat1000.m	AQUAtec function, slightly adapted, to convert ABS data from *.aqa to *.mat.	exportConvertABS.m
RemoveAboveSurface.m	(ABS data) Clears signal above surface range.	ABSinversion.m
resoFreq.m resoRadius.m	Computes resonance frequency (resp. radius) for a given radius (resp. frequency) (equation 5.13)	Many
SeparateMvAtt.m SeparateMvAtt2.m	(ABS data) Iterative process to extract M_v and $10^{-2 \cdot att}$ from the data	ABSinversion.m
simuDisp.m	Calculates the values u and v from [5]	simulationScript.m
simuDistrib.m	Creates an artificial set of bubbles distribution n	simulationScript.m
simuInterp.m	This function interpolate a given set of points with hat functions	simulationScript.m
simuInversion.m	To tune Tikhonov parameter λ (Function version of simulationScript.m)	simulationIter.m
simuKernel.m	Computes the kernel complex function K	simulationIter.m
simuKPhi.m	Computes the integrated product $\int_a K \varphi$ (see equation 7.6)	simulationIter.m
simuPhi.m	Computes the hat functions φ (see equation 7.5)	simulationIter.m
SurfaceRangeIndex.m	(ABS data) Finds surface range index	ABSinversion.m
TimeFiltering.m	(ABS data) Applies a median filter on the proposed signal along time (see function RangeFiltering.m)	ABSinversion.m
VolumeG.m	Computes volume V_G according to equation 1.11	ABSinversion.m
Xi.m XiAquatec.m	Near range factor from [8] and [4] respectively	misc_calculations.m

Data

Name	Description	In the report
aqABS_chara.mat	Contains characteristics of ABS provided by AQUAtec. Loaded by loadAquatecData.m	Table 3.1

Bibliography

- [1] J. Parente Da Silva, “Acoustic methods for assessment of bubbles produced by marine plants,” 2018.
- [2] H. Medwin and C. S. Clay, *Fundamentals of acoustical oceanography*, ser. Applications of Modern Acoustics. Academic Press, 1997.
- [3] S. Vagle and D. M. Farmer, “The measurement of bubble-size distributions by acoustical backscatter,” *Journal of Atmospheric and Oceanic Technology*, vol. 9, no. 5, pp. 630–644, 1992.
- [4] AQUAtec, “Application note AN4,” 2013, available in AQUAtec CD.
- [5] K. W. Commander and A. Prosperetti, “Linear pressure waves in bubbly liquids: Comparison between theory and experiments,” *The Journal of the Acoustical Society of America*, vol. 85, no. 2, pp. 732–746, 1989.
- [6] P. Felisberto, J. Parente Da Silva, and A. Silva, “EPPO preliminary tank experiment Data report,” 2016.
- [7] L. Gostiaux and H. van Haren, “Extracting meaningful information from uncalibrated backscattered echo intensity data,” *Journal of Atmospheric and Oceanic Technology*, vol. 27, no. 5, pp. 943–949, 2010.
- [8] A. Downing, P. D. Thorne, and C. E. Vincent, “Backscattering from a suspension in the near field of a piston transducer,” *The Journal of the Acoustical Society of America*, vol. 97, no. 3, pp. 1614–1620, 1995.
- [9] M. A. Ainslie and T. G. Leighton, “Review of scattering and extinction cross-sections, damping factors, and resonance frequencies of a spherical gas bubble,” *The Journal of the Acoustical Society of America*, vol. 130, no. 5, pp. 3184–3208, 2011.
- [10] T. K. Stanton, “Simple approximate formulas for backscattering of sound by spherical and elongated objects,” *The Journal of the Acoustical Society of America*, vol. 86, no. 4, pp. 1499–1510, 1989.
- [11] R. Duraiswami, S. Prabhukumar, and G. L. Chahine, “Bubble counting using an inverse acoustic scattering method,” *The Journal of the Acoustical Society of America*, vol. 104, no. 5, pp. 2699–2717, 1998.
- [12] C. Hansen. (2008) Regularization Tools, A Matlab Package for Analysis and Solution of Discrete Ill-Posed Problems. Version 4.1 for Matlab 7.3. [Online]. Available: www.mathworks.com/matlabcentral/fileexchange

- [13] A. Tikhonov, A. Goncharsky, V. Stepanov, and A. Yagola, *Numerical Methods for the Solution of Ill-Posed Problems*, ser. Mathematics and Its Applications. Springer Netherlands, 1995.
- [14] K. F. Betteridge, P. D. Thorne, and R. D. Cooke, “Calibrating multi-frequency acoustic backscatter systems for studying near-bed suspended sediment transport processes,” *Continental Shelf Research*, vol. 28, pp. 227–235, 2008.